UNIVERSIDADE DE SÃO PAULO
INSTITUTO DE FÍSICA DE SÃO CARLOS

Tales Ferraz de Paula

Search for exotic particles (Q-balls) in ultra-high-energy Astroparticles

São Carlos

2023

Tales Ferraz de Paula

Search for exotic particles (Q-balls) in ultra-high-energy Astroparticles

Dissertation presented to the Graduate Program in Physics at the Instituto de Física de São Carlos da Universidade de São Paulo, to obtain the degree of Master in Science.

Concentration area: Theoretical and Experimental Physics

Advisor: Prof. Dr. Luiz Vitor de Souza Filho

Corrected version

(Original version available on the Program Unit)

São Carlos

2023

ACKNOWLEDGEMENTS

"I have seen the dark universe yawning
Where the black planets roll without aim,
Where they roll in their horror unheeded,
Without knowledge, or lustre, or name. "
— **H. P. Lovecraft**

"There is no path...
Beyond the scope of light, beyond the reach of dark... what could possibly await us?
And yet, we seek it, insatiably. Such is our fate."
— **Aldia, Scholar of the First Sin**

ABSTRACT

PAULA, T. F. **Search for exotic particles (Q-balls) in ultra-high-energy Astroparticles**. 2023. 89p. Dissertation (Master in Science) - Instituto de Física de São Carlos, Universidade de São Paulo, São Carlos, 2023.

This dissertation was proposed in the scenario of studying candidates for the origins of ultra-high-energy cosmic rays. The main goal is to study exotic air showers induced by Q-balls and to develop a method to differentiate exotic-induced air showers from proton-induced ones in the energy range from $10^{17.0}$ to $10^{21.0}$ eV. The first part of the study was done with the analysis of longitudinal profiles of air showers simulated with CONEX for more than seventeen thousand events simulated. In the second part, a method is proposed that is compatible with the event-analysis chain of the Pierre Auger Observatory. The first results are divided in three parts, based on the three simulation groups that were done. The first result from the simulation study allowed the proposal of another fit function hypothesis to describe the exotic-induced shower, along with the Gaisser-Hillas function, typically used to describe the profile of hadronic-induced showers. The second result allowed a fully unambiguously classification based on the goodness-of-fit method χ^2/ndf value when comparing both fitted functions for each primary particle. The third result from simulated events analysis showed independence of energy deposit rate from primary energy for exotic-induced showers, allowing a parametrization proposal for the energy deposit rate with Q-ball's cross-section. The second part of results was to apply the proposed method to Pierre Auger Observatory, by testing it on the Observatory's $\overline{\text{Off}}\underline{\text{line}}$. A new module was proposed for it and a initial test was performed. It is shown that, even after taking into account all the detector and geometry effects related to the fluorescence-based detection of extensive air showers, the classification of exotics is still possible, hinting to the success of the method. Further study, however, is necessary to fully test and validate the method, and the next steps were then discussed.

Keywords: Extensive air shower. CONEX simulation. Cosmic rays.

RESUMO

PAULA, T. F. **Busca por partículas exóticas (Q-balls) em Astropartículas ultra-energéticas**. 2023. 89p. Dissertação (Mestrado em Ciências) - Instituto de Física de São Carlos, Universidade de São Paulo, São Carlos, 2023.

Esta dissertação foi proposta no intuito de estudar candidatos às origens de Raios Cósmicos ultra-energéticos. O objetivo principal é estudar exóticos chuveiros atmosféricos extensos iniciados por Q-balls, e desenvolver um método para diferenciar chuveiros exóticos de chuveiros iniciados por prótons no intervalo de energia de $10^{17.0}$ a $10^{21.0}$ eV. A primeira parte do estudo compreende toda a análise de perfis longitudinais de chuveiros atmosféricos simulados com CONEX, com mais de dezessete mil eventos simulados. Na segunda parte, um método compatível com a análise de eventos do Observatório Pierre Auger é proposto. A primeira parte dos resultados é dividida em três, baseada nos três grupos de simulações realizados. O primeiro resultado do estudo das simulações permitiu a proposta de outra hipótese para função de ajuste para chuveiros exóticos, junto da função de Gaisser-Hillas, tipicamente utilizada para descrever o perfil de chuveiros hadrônicos. O segundo resultado permitiu uma classificação inequívoca baseada no valor do método de qualidade de ajuste χ^2/ndf quando comparadas ambas funções de ajuste para cada partícula primária. O terceiro resultado da análise dos eventos simulados mostrou independência da taxa de depósito de energia com energia primária para chuveiros exóticos, permitindo uma proposta de parametrização com a taxa do depósito de energia com a seção de choque do Q-ball. A segunda parte do estudo foi a aplicação do método proposto no Observatório Pierre Auger, com teste deste no software $\overline{\text{Off}}\underline{\text{line}}$ do Observatório. Um novo módulo foi proposto para a aplicação e um teste inicial foi realizado. Mesmo considerando os efeitos de geometria e do detector relacionados com a detecção de chuveiros atmosféricos extensos baseada na luz de fluorescência, foi possível uma classificação dos chuveiros exóticos, indicando sucesso do método. Estudos posteriores, porém, são necessários para um teste completo e validação do método. Assim, os próximos passos foram discutidos.

Palavras-chave: Chuveiros atmosféricos extensos. Simulação com CONEX. Raios cósmicos.

LIST OF FIGURES

LIST OF TABLES

CONTENTS

1 INTRODUCTION

Astroparticle physics, or particle astrophysics, is a high-energy field of study that tries to provide an answer to one of the most extreme energetic events in the universe: the origins of ultra-high-energy charged cosmic radiation, the ultra-high-energy cosmic rays. To answer this question, studies of composition, acceleration and sources are necessary, but very difficult to do, from an experimental perspective, given the extreme rarity of these events and the indirect possible measurements. These astroparticles arrive at Earth with a vast energy range that can be higher than possible by human-made accelerators, and leave a footprint in Earth's atmosphere: an Air Shower. These showers can be detected by different techniques, but the ultra-high-energy astroparticles starts Extensive Air Showers — events that only extensive terrestrial observatories can indirectly detect.

The extensive air shower is a cascade of particles initiated by the primary astroparticle. This cascade carries out information regarding the primary particle and provide access to these ultra-high-energy range, otherwise inaccessible.

Going back to the fundamental question of the origins of these rare events, among many candidates, there are exotic particles. Exotic particles are those that behaves differently from ordinary matter, and, in most of the cases, violate one law of physics. However, these particles could serve as an origin for the ultra-high-energy cosmic rays, as will be described in this dissertation. This work will focus on one exotic, specifically in the exotic Q-ball, and will be based on simulations done in Extensive Air Showers produced by it using CONEX.

This research will explore the possibility to find exotic particles, Q-balls, within ultra-high-energy cosmic rays. The goal will be approached by choosing an statistical method to study and classify simulated exotic-induced air showers by comparing with proton-induced ones. The method will be evaluated and applied to the Pierre Auger Observatory, in order to test it.

This work is divided in an introductory part, from Chapters 2 to 5, were an overview of import and relevant study areas is given, and a results part, comprehending Chapters 6 and 7, were this dissertation's results are presented and studied. The following sections summarizes each chapter aforementioned.

In Chapter 2, ultra-high-energy cosmic rays, an overview is given to these charged astroparticles. Starting from its history, going through some early experimentation to quick citation of the modern observatories that operate in their range, then to the cosmic ray energy spectrum, were its shape and other parameters are described, and finalizing with phenomena, origin and acceleration processes and other characteristics. This chapter

is dedicated to provide a base to what will be discussed in the next chapters, as well to provide basic insight about the field.

In the following Chapter 3, Extensive Air Showers, still with the aim of providing the necessary tools to this work, the air shower phenomenology, along with its components, is presented. The basic observables are given a theoretical overview, and the electromagnetic and hadronic cascades are presented. Finally, the simulation of air shower events is addressed — the main tool of this work.

Chapter 4, the Pierre Auger Observatory, presents the observatory that this dissertation will work with. A general overview of its detectors, the Surface and Fluorescence Detectors, is given, presenting general characteristics of each one and their trigger level system.

Narrowing down the exotic particles field, Chapter 5 presents the peculiar Q-ball. A theoretical overview is provided, along with its interaction with matter and previous work with Q-balls and air shower simulation. Lastly, Q-ball-induced and proton-induced air showers simulation is referred in the last section, guiding to the results chapters that will follow.

In Chapter 6, Exploring Longitudinal Profile Shape Information, the χ^2/ndf statistic is presented as the statistical method to differentiate and classify simulations of Q-ball-induced and proton-induced air showers. These air showers longitudinal profiles are fitted with two proposed functions and its fit results, given by χ^2/ndf, are analyzed. The good results of the proposed method allows it to be taken into the Pierre Auger Observatory, were a initial test and validation is done. A parametrization of the energy deposit rate and Q-ball cross-section is also presented, arriving from this exotic-induced air shower longitudinal profile study.

Chapter 7, Exploring Longitudinal Profile Shape Information Including Observatory Simulation, presents the application of the proposed method into the Pierre Auger Observatory. This is done to study the method when working with reconstructed data by the Observatory — that comes with its instrumental limits. Despite the addition of these uncertainties, the results are promising, as they corroborate with the previous chapter.

Lastly, in Chapter 8, Final Thoughts and Future Perspectives, the entire research work and its results are presented in a summarized way. The next steps, future work and validation steps to the method are then presented.

2 ULTRA-HIGH-ENERGY COSMIC RAYS

With an energy range going up to 10^{21} eV, single extraterrestrial, and even extragalactic, particles can reach and interact with Earth's atmosphere particles, giving us a taste of extremely violent environments from the Universe. These energetic particles are denoted cosmic rays, and the extreme values above $\sim 10^{17}$ eV correspond to Ultra-High-Energy Cosmic Rays (UHECR). Their interactions can lead to cascade reactions in the atmosphere, the so called air showers. Whereas UHECR are theorized to be produced in the most energetic extragalactic environments, the study of it is, therefore, a fundamental piece of the puzzle to better understand the Universe, both on a microscopic and macroscopic scales. However, since the UHECR energy range is much beyond the achievable by human-made accelerators, their study rely on the detection by observatories and simulations by Monte Carlo techniques — experimentation on accelerators is still out of reach.

The Pierre Auger Observatory localized in Argentina is currently the largest detector in the world designed to detect UHECR. The Telescope Array, United States, and the Akeno Giant Air Shower Array (AGASA), Japan, are other examples of observatories that detect UHECR. Together, their data has already provided significant advances in the field of astroparticle physics.

In the next Section, a historical overview about cosmic rays will be presented, followed by some detailed discussion about the cosmic rays flux, energy, sources and acceleration.

2.1 A Brief History of Cosmic Rays

In 1910, Theodor Wulf measured a reduced intensity of radiation in an electrometer at the top of Eiffel tower. This reduction, however, was not as severe as it was theorized with Earth being the only source of radiation; the ionization of the air was greater than expected, pointing to another radiation source. (1)

Between 1911 and 1913, Victor Hess, believing that the source for Wulf's unexpected ionization profile was in the sky, made a series of high-altitude balloon flights to prove his theory. Surprisingly, he found that it was indeed an odd ionization profile: there was a sharp increase of it at higher altitudes! He continued his experiments and flew at day, at night and during a partial solar eclipse — no significant difference in the radiation levels was found. From these experiments, the Sun was discarded as the major possible source, and he concluded that these radiations should be originated at greater distances. (2) This discovery awarded Hess the 1936 Nobel Prize in physics, and his accomplishments are

commonly regarded as the starting point of astroparticle physics.

Robert Millikan, in 1925, was the first to use the term "cosmic rays" to refer to the cause of this radiation, believing that it was composed of gamma rays. (3) This, however, was refuted in 1933, in Jacob Clay's work; while traveling from Holland to East Indies in a expedition, Clay showed the dependency of the flux of cosmic rays on latitude, implying that the particles were being influenced by Earth's geomagnetic field and, hence, must be electrically charged. (4)

Bruno Rossi, in 1930, predicted that there should be a difference in the flux of cosmic rays coming from the east when compared to the west, given the Earth's field orientation. (5) The effect, named *east-west effect* was proved by the works of Thomas Johnson (6) and Luis Alvarez and Arthur Compton (7), both in 1933.

With the use of cloud chambers to study cosmic rays, still in 1933, the positive electron was discovered by Carl Anderson (8) and later, together with Seth Neddermeyer, in 1937, the muon was discovered. (9) These discoveries mark the beginning of the elementary particle physics, and cosmic rays were used in that area until 1950's, when particle accelerators became reality.

Back to the 1930's, with the advance in experimental techniques, and with the new particles discovered, the idea of a single energetic gamma ray reaching the ground from extraterrestrial sources gave place to the concept of a cascade of interactions initiated by a energetic *primary particle*. The product of these interactions were *secondary* electrically charged particles. Showers of particles moving in approximately the same direction were being observed in cloud chambers, and the idea of air showers started to develop.

Rossi, during his work on the *east-west effect* noticed a trigger in coincidence in his Geiger counters instruments that it was above the rate expected by random noise. He postulated on his field report that the cause could be due to a very extensive particle shower, but did not pursue the subject further. (10) Only in 1937, unaware of Rossi's notes, Pierre Auger, with his group, performed an experiment distributing Geiger counters horizontally to measure horizontal coincidence events of cosmic-ray-induced showers. Auger and his group found out cosmic rays correlated in time separated by great distances and concluded that this was being caused by showers of particles initiated by a single cosmic ray. Calculations based in their results revealed that these Extensive Air Showers (EAS), as called today, had energies in the range of 10^{15} eV (11 - 12), extending the upper limit of energy yet predicted and observed. (13) Thus, the high-energy astroparticle physics field was born.

Following the discoveries of Auger and his group, in the next decades, works to measure the properties of cosmic rays — *e.g.* mass composition, arrival time and direction and energy spectra, were made. John Linsley in 1959 made a pioneer work and began the

era of ground arrays (14) and, in 1963, presented his results; measurements of EAS with energies from 10^{17} to 10^{20} eV. (15, 16) These new values again pushed the upper limit if the energy spectrum of cosmic rays. A particle with such a energy is extremely rare; its flux is less than one particle per square kilometer per century!

Linsley's work paved the way to ground arrays; the Fly's Eye experiment, (17) AGASA, (18) Sydney University Giant Air Shower Recorder, (19) Haverah Park experiment, (20) Yakutsk array, (21) and the other two aforementioned Pierre Auger Observatory (22) and the Telescope Array (23) are examples of ground arrays observatories that followed his work.

After the discovery of the Cosmic Microwave Background radiation (CMB), in 1966, the works of Greisen (24) and Zatsepin and Kuzmin (25) independently predicted that protons with higher kinect energy than $\sim 4 \times 10^{19}$ eV would undergo photo-pion production, by interacting with the 2.7K CMB photons. The so-called GZK effect was confirmed by the updated Fly's Eye experiment, High Resolution Fly's Eye (HiRes) (26) and PAO. (27) If one considers the astrophysical model were the primary flux at this energy is dominated by protons, this production would strongly suppress the cosmic ray flux above this energy.

In the present scenario, the completeness of the sky is covered in the ultra-high-energy range by collaboration of researchers and the Pierre Auger Observatory and Telescope Array. Many advances were made; the energy spectrum is precisely described and measured, (28) simulation techniques provide access to energies above the limits of humankind and studies on the mass composition have already been made . (29–33) Nevertheless, the question remains unanswered: what are the origins to ultra-high-energy cosmic rays? A possible candidate for this question will be discussed later in this work. Below, the energy spectrum of cosmic rays will be discussed.

2.2 The Energy Spectrum

Precisely measured, the energy spectrum of cosmic rays ranges from 10^8 to 10^{20} eV. In the UHECR range, the number of incident particles on Earth greatly falls from 1 m^{-2} yr^{-1} eV^{-1} to less than ~ 0.01 km^{-2} eV^{-1} per century. Figure 1 presents the all-particle spectrum scaled by a factor of $E^{2.6}$: a compilation of measurements from several experiments. Its shape roughly follows an inverse power law

$$\frac{dN}{dE} \propto E^{-\alpha} . \tag{2.1}$$

Four well-established features can be seen in the cosmic ray spectrum: the two "*knees*" — the second one being more recent — the "*ankle*" and the suppression. These features are characterized by changes in the spectral index α. Up to the first knee ($E \sim 10^{15}$ eV), the spectrum is well described with $\alpha \approx 2.7$, where it steepens to $\alpha \approx 3$, followed by
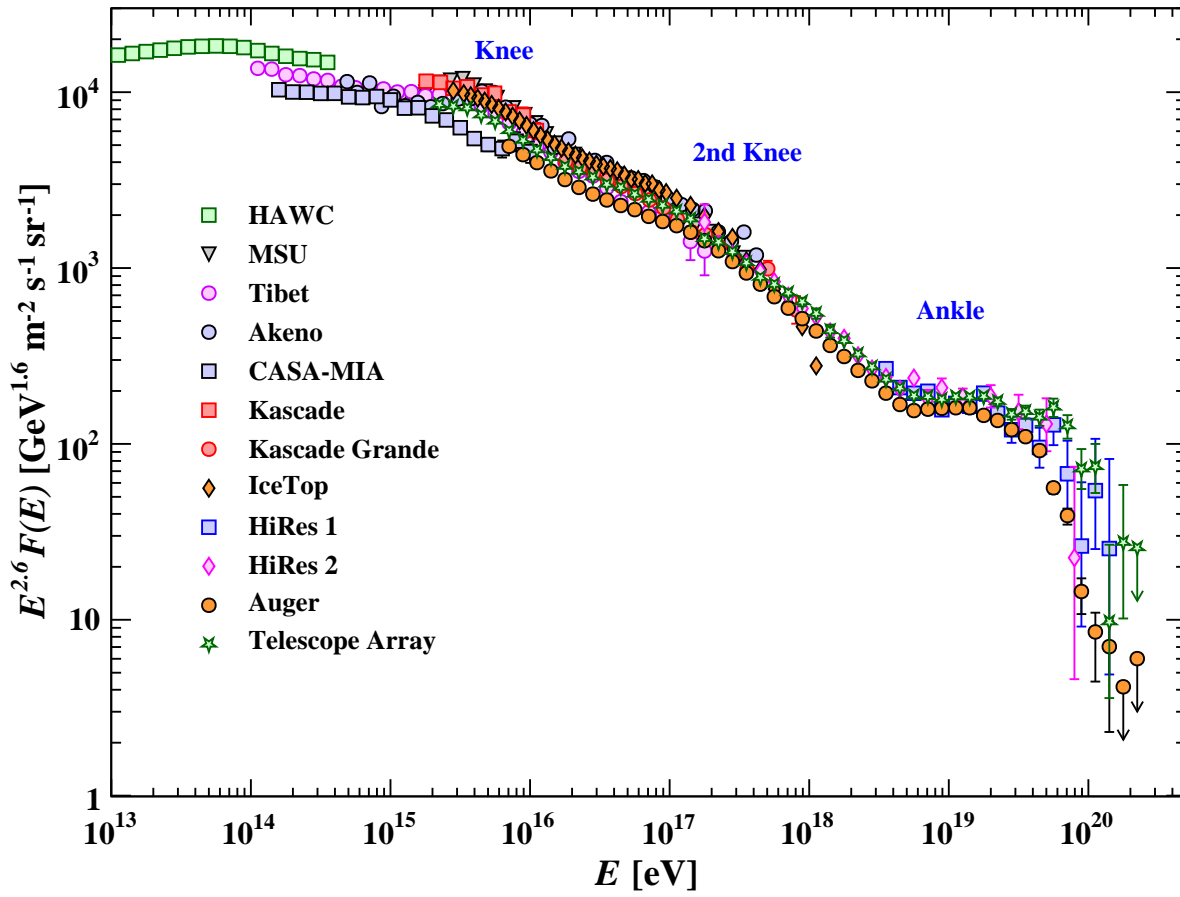
Figure 1 – All-particle energy spectrum.
Source: WORKMAN *et al.* (39)

a second steepening at $E \sim 10^{17}$ eV — the second knee — with $\alpha \approx 3.3$. Finally, around 5×10^{18} eV a hardening occurs, the ankle, with $\alpha \approx 2.5$. (34–38) The suppression of the flux, however, is another well-established feature (see Section 2.3).

This shape of the energy spectrum and the changes in α carry information regarding the source and acceleration of cosmic rays and the dynamics of the environments in which they traverse. The features of the cosmic ray spectrum are still a matter of debate and active areas of study in astroparticle physics. Further discussions regarding the energy spectrum will be discussed in the next session, alongside the composition, origins and acceleration mechanisms of cosmic rays.

2.3 Sources, Composition and Acceleration of Cosmic Rays

Direct measurements of particle composition is possible above the first knee (from energies from 10^9 up to 10^{15} eV) by high altitude detectors —*e.g.* balloons or satellites. This is achievable thanks to the high flux and low energy of particles. This composition is believed to be mainly of free protons and ionized helium. Below this energy range, the

flux of particles is dominated by solar and geomagnetic effects — particles with these low energies ($< 10^9$ eV) are diffused from Earth by solar wind and geomagnetic field. At energies above 30 GeV, however, these effects are extremely low and the flux begins to rise. The Sun and similar stars are said to be the possible sources to these particles. (37, 40 - 41)

The composition of cosmic rays below the knee region is mainly of protons and light elements, like helium, and other medium to heavier elements, like carbon, nitrogen and iron. Local sources shift to more distant galactic sources, as the heavier nuclei starts to appear more.

The approximately constant spectral index of the all-particle up to the first knee is given by a combination of the spectrum of nuclei and the long effect of diffusion by the magnetic field and galactic winds. (37,42 - 43) From the many possible acceleration mechanisms for cosmic rays up to $\sim 10^{17}$ eV, shock acceleration by supernova remnants — called second order Fermi acceleration — are the most probable one. It consists of moving magnetized plasmas in the form of the expanding shock fronts from supernovae explosions in which particles are accelerated by stochastically scattering and should produce a power law. (37, 41, 44)

Beyond the first knee energy, the flux quickly drops, and the detectability of cosmic rays become indirect; ground arrays, like the Pierre Auger Observatory, take place. From this energy to the higher end, measurements are done by studying the results of cosmic rays interactions in the atmosphere, the air showers.

The ankle region represents a hardening in the flux. Although this is still an area of debate, (45) a possible cause for it is the opposite of what happens in the knee scenario: extragalactic particles arriving in our galaxy, with the highest energies. (16, 37, 46) Only giant ground arrays can collect enough data to study these regions. Data from the Pierre Auger Observatory suggest that the composition is a transition from light to heavier elements. (30 - 31, 38, 47) The exact transition to extragalactic flux is still undetermined.

Beyond the ankle, much is unknown; direct observation is unachievable and even the indirect observation is difficult. Extrapolation from the energy range from particles accelerators gives the only interaction models obtainable at the time — and they come with huge uncertainties. It is well-established, however, that a suppression in the cosmic ray flux occurs past the ankle, as shown in Figure 1. Its exact energy value is not precisely defined, as both Pierre Auger Observatory and Telescope Array disagree with each other, between 5×10^{19} (38) and 6.5×10^{19} eV, (48) respectively, even when accounting for systematic errors. This disagreement it is not only because measurements differences, but also because the hybrid detection aspect of the Pierre Auger Observatory.

In a more present scenario, this suppression, or cutoff, is explained either by the
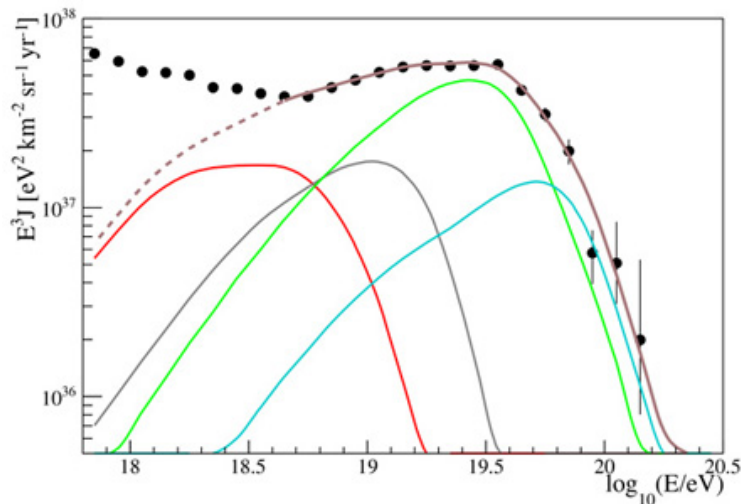
Figure 2 – Reproduction of the Pierre Auger Observatory data (filled circles) with the simulated fitted energy spectrum. The partial spectra are Hydrogen (red), helium-like (grey), carbon, nitrogen, Oxygen (green), aluminum-like (cyan), iron-like (blue), total (brown).
Source: AAB *et al.* (49)

GZK effect, mainly affecting protons, or by photo-dissociation in the case of nuclei, with CMB photons and by the end of the power of the sources. Based on the mass-composition data from the Pierre Auger Observatory presented in Figure 2, the end of the spectrum should be composed by a mixed composition if current hadronic interaction models are well-suited for describing air shower physics.(29) The GZK effect for protons can result in pair and photo-pion production, as follows:

$$p + \gamma_{CMB} \rightarrow p + e^+ + e^- \,, \tag{2.2}$$

$$p + \gamma_{CMB} \rightarrow p + \pi^0 \,. \tag{2.3}$$

Heavier nuclei can undergo in the process above, but with much smaller frequency. The main effect in the interaction with CMB photons, and also the infrared, optical and ultra-violet photons — Extragalactic Background Light (EBL) —, is photo-dissociation:

$$A + \gamma_{CMB,EBL} \rightarrow (A - N) + N \,. \tag{2.4}$$

These particles should be accelerated by mechanisms such as Active Galactic Nuclei (AGN) — that are said to have the necessary size and magnetic field —, and encountering coronas from galactic collision should produce first order Fermi accelerations powerful enough. Others examples are neutron stars, gamma-ray burst, large-scale galactic shocks and even exotic particle decay. (44)

Another difficulty for pointing out the origins of UHECR is their anysotropy. As they have charge, they are scrambled by magnetic fields across their journey through the cosmos, making source correlation unachievable — even the most energetic ones.

Because the study of these energetic particles cannot be done directly, unambiguous data regarding the mass composition of the by-product of their interactions is not yet available. If they become available, the astrophysical models that describe the UHECR region would strongly be reduced, based on the chemical abundance of this data.

3 EXTENSIVE AIR SHOWERS

After traversing the cosmos with trajectories that go from nearly straight to total scrambled, the highly energetic cosmic rays can reach Earth's atmosphere and interact with air nuclei — mainly constituted of nitrogen, oxygen and argon. Upon the first interaction, based on the current hadronic interaction models, this energetic cosmic ray, now referred as *primary particle*, start an *Extensive Air Shower* (EAS) in the upper atmosphere, where many *secondary particles* are generated after the first interaction. These secondaries also starts sub-processes, by decay or interaction, producing more and more secondaries, repeating this sub-process that rapidly gives rise to a large cascade of reactions, that grows in number and decreases the energy per particle. This production persists until the energy per particle is not enough to maintain particle production, and particle absorption process quickly dominates. At this point, the maximum number of particles in the cascade is achieved, referred as shower maximum. The cascade then starts to fade, and the long survivors, radiation or decay/interaction product at last reach the ground, ceasing the process. The shower has three main components; hadronic, electromagnetic and muonic, as shown by Figure 3 and can be divided between pure electromagnetic cascades, initiated by photons or electrons/positrons, and hadronic cascades, initiated by nuclei or any type of hadron.

This simplified description of the EAS will be the basis for the next sections, where the EAS principal components will be described with more detail. Sections 3.1 and 3.2 will start with the descriptions of phenomenology and observables from EAS. Next, Sections 3.3 and 3.4 will provide a description of the different cascades, together with its heuristic models and, lastly, Section 3.5 will be focused on the computational simulation available for EAS, with emphasis to the methods applied in this work.

3.1 Basic Phenomenology

After interacting with an air nuclei, typically between heights from 15 to 35 km, the primary gives rise to the secondary particles and starts the EAS, that can be divided in three main components: the hadronic, the electromagnetic and the muonic.

Neutral and charged pions are the most frequent ones produced, followed by kaons and baryons. The neutral pion immediately decays into a pair of photons, mainly feeding the electromagnetic component. Charged pions and kaons have a greater lifetime and can interact again, before decaying into muons and neutrinos. Together with baryons, they form the hadronic core component of the shower and produce about 90% of the muons.

The electromagnetic component is composed of photons and electrons/positrons
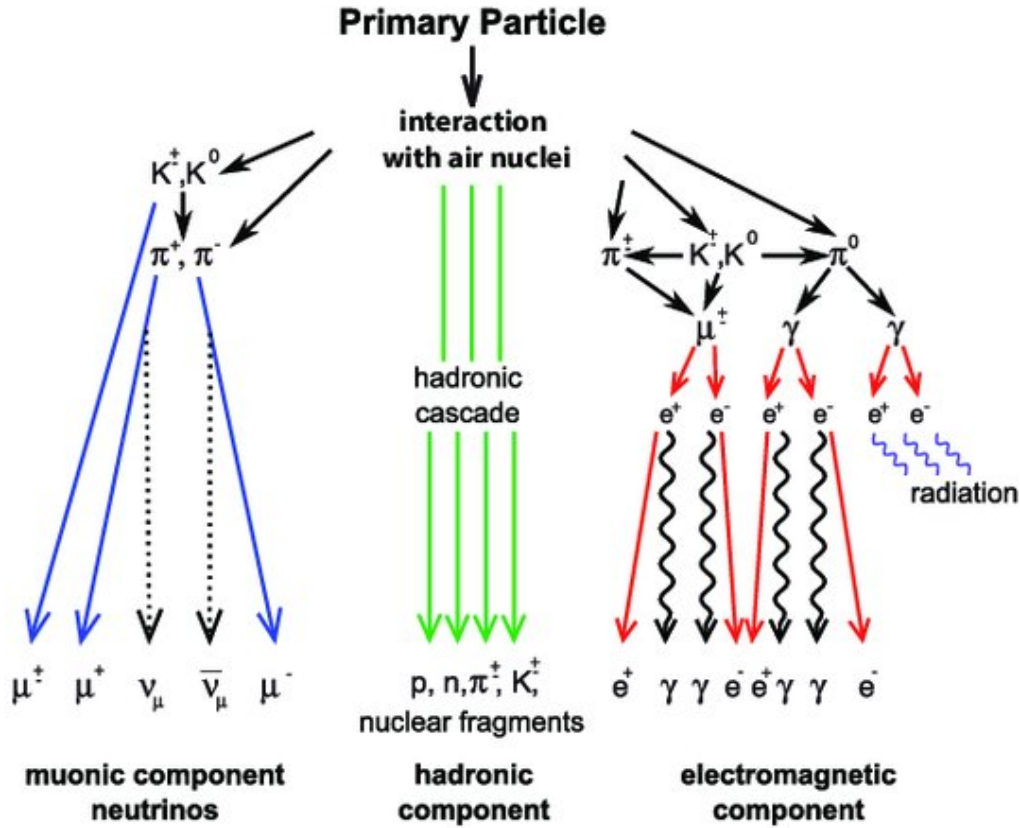
Figure 3 – Schematic view of the three main components of Extensive Air Showers and its interactions.
Source: HAUNGS *et al.* (50)

generated via pair production. These particles will continuously produce one another through pair production and *bremsstrahlung* until the electron/positron energy fall bellow the critical energy ϵ_{crit}^e in air, at which ionization energy loss equals the aforementioned process energy loss. Based on Heitler model and Greisen profile, the number of electrons can be used for estimation of primary energy (see Section 3.3).

Finally, the muon component of the EAS can propagate through the atmosphere with less interactions and energy loss, reaching the ground with small attenuation. Based on the superposition model, (51,52) the depth of maximum muon production can be used for estimation of primary composition (see Sections 3.2 and 3.4).

3.2 Basic Observables

The *primary energy*, E_0, and *primary mass composition* are parameters of great importance, as they will greatly determine the amount of particles produced in the shower and its development. They cannot be measured directly, since only the left-over of shower reach the detectors, but can be estimated by comparison with simulation predictions
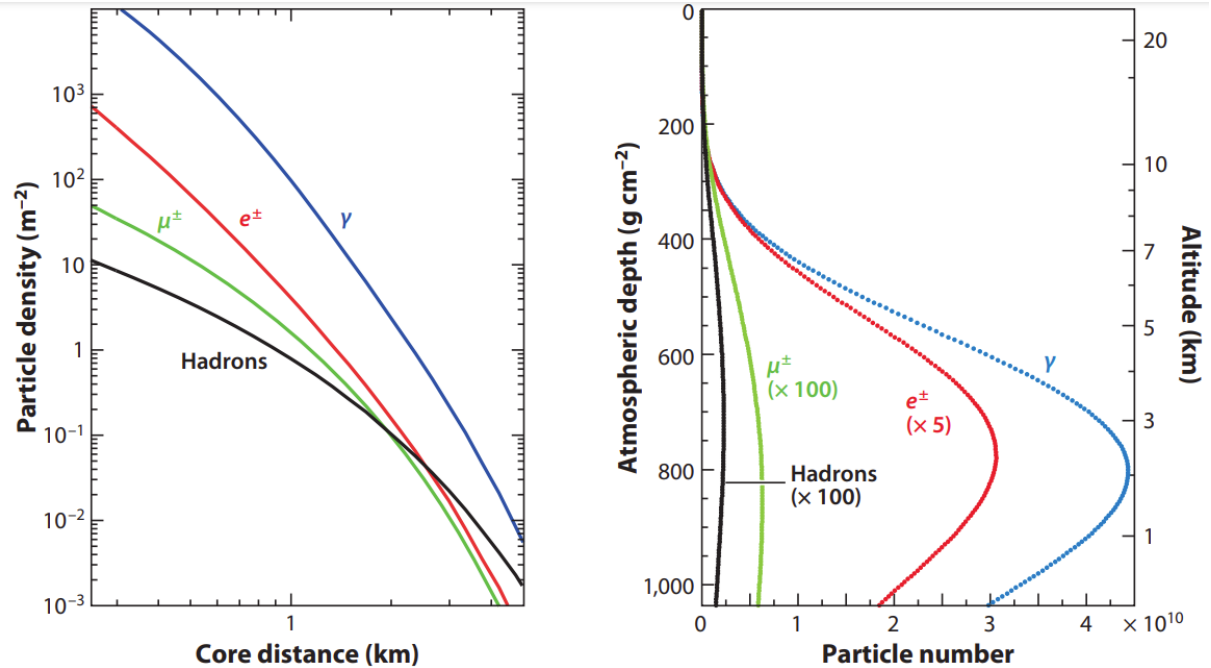
Figure 4 – Average simulation results of $10^{19}\,eV$ vertical proton-induced showers. *Left: lateral distribution at* $870\,g/cm^2$. *Right:* Longitudinal profile.
Source: ENGEL; HECK; PIEROG. (51)

and reconstruction of events in the observatories (see Chapter 4, Section 4.3) via the *longitudinal profile* and *lateral distribution*, as shown in Figure 4. Simulation provides a great source of systematic uncertainties in the interpretation of cosmic rays, because they are dependent on theoretical models. From the two main process of air showers particle production, the electroweak interaction is well understood, whereas the hadronic production is subject to theoretical uncertainties. (53)

The longitudinal profile gives the number of particles, $N(X)$, as a function of the amount of matter that the shower has passed through, the *slant depth* X, in g/cm^2, from the top of the atmosphere. But it can also provide the energy deposit rate (see Chapter 4), giving a great estimator for the primary energy. X is related to the vertical atmospheric depth X_{atm} and zenith angle θ, for $\theta \leq 60°$, (54) of the incoming primary via

$$X = \frac{X_{atm}}{\cos\theta}, \tag{3.1}$$

where X_{atm} is the amount of matter that the primary particle has vertically passed through in which it has started an air shower, given by the integral of the atmospheric density above the observation level h. (55)

$$X_{atm}(h) = \int_h^\infty \rho(h')dh'. \tag{3.2}$$

The zenith angle greatly influences air shower development: as the air shower evolves in the atmosphere, the number of particles in the shower and their lateral spread increase. At
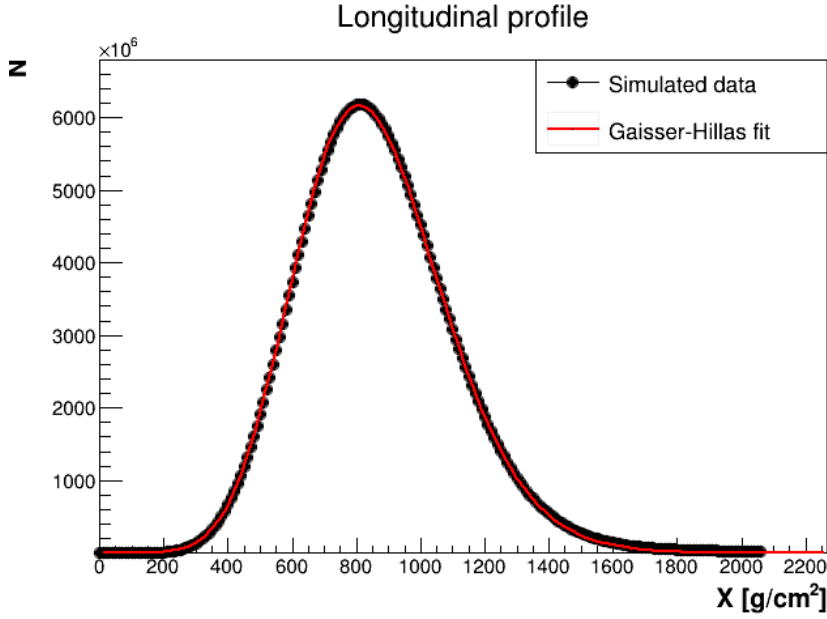
Figure 5 – Simulated Extensive Air Shower by CONEX initiate by a vertical proton with primary energy of $10^{19.0}\,eV$ with a Gaisser-Hillas fit.
Source: By the author.

larger zenith angles, the shower becomes more elongated and wider due to the increased path length and the greater number of interactions. Additionally, the density of the atmosphere increases as the zenith angle decreases, leading to more frequent particle interactions.

The longitudinal profile can be described by the Gaisser-Hillas function for EAS, (56) as seen in Figure 5. In this form, the function relates $N(X)$ to the maximum number of particles (N_{max}) at shower maximum (X_{max}) and the parameters λ and X_0 in an empirical manner such as

$$N(X) = N_{max} \left(\frac{X - X_0}{X_{max} - X_0} \right)^{\frac{X_{max} - X_0}{\lambda}} \exp \left(\frac{X_{max} - X}{\lambda} \right) . \tag{3.3}$$

The two fit parameters relate to the curve's shape, with λ describing shower width and X_0 a pseudo first interaction depth without physical meaning.

The total number of charged particles is obtained by a radial integration of the fitted radial fall-off of the measured particle densities. This lateral distribution of particles is caused mainly by multiple Coulomb scattering of electrons off atmospheric atoms spread the shower. This Lateral Distribution Function (LDF) has a large variety, but a generalization, for electromagnetic cascade, is found to be the known Nishimura-Kamata-Greisen (NKG) function: (57, 58)

$$\rho_{NKG}(r, s, N_e) = \frac{N_e}{r_M^2} \frac{\Gamma(4.5 - s)}{2\pi \, \Gamma(s) \, \Gamma(4.5 - s)} \times \left(\frac{r}{r_M} \right)^{s-2} \left(1 + \frac{r}{r_M} \right)^{s-4.5} , \tag{3.4}$$
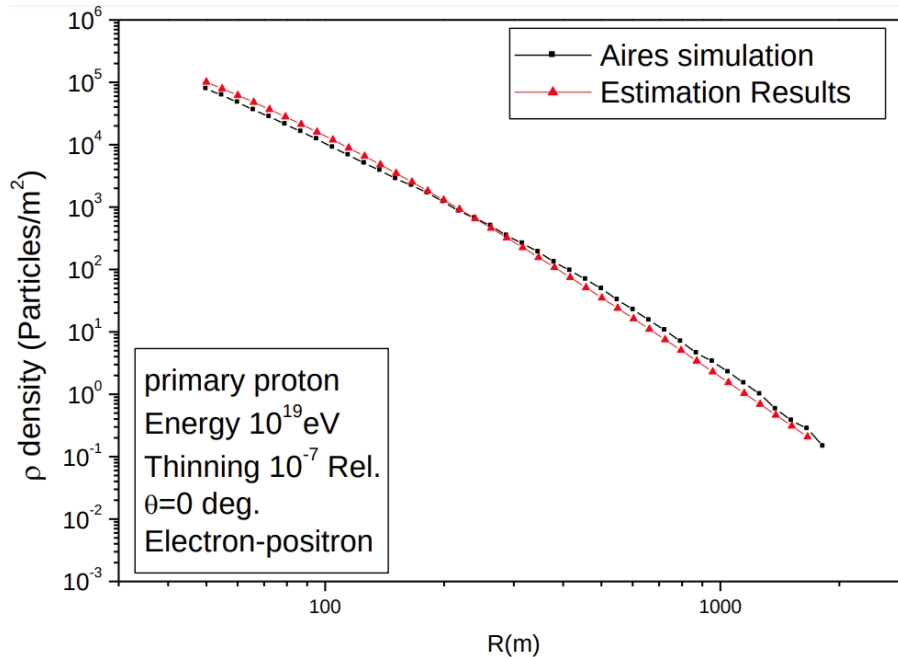
Figure 6 – Simulated lateral distribution for a electromagnetic air shower initiated by a vertical proton with primary energy of $10^{19}\,eV$ with a Nishimura-Kamata-Greisen fit.
Source: FADHEL *et al.* (60)

with r_M being the Molière radius, N_e the total number of electrons in the shower and s the shower age (for this form, $0.5 < s < 1.5$). (52) The shower age s arises from cascade theory, (59) describing how particles evolve in the atmosphere, and is calculated by

$$s = \frac{3X}{X + 2X_{max}}.\qquad(3.5)$$

As can be seen in Figure 6, the NKG function presents a good agreement with simulated profiles. The lateral distribution provides the particle density at observation level X and is useful for giving a good estimate of primary energy, independently of primary composition, based on the number of charged particles (see next section), and primary mass composition, based on the number of muons (see Section 3.4).

3.3 Electromagnetic Cascade

A pure electromagnetic cascade is induced by a photon or by an electron or positron and can be loosely approximated by the Heitler toy model (61), first introduced by (62), for basic shower development understanding. This model assumes a simple branching development for the shower, where one particle with energy E_0 interaction results in two new particles with $E_0/2$ each. In case of an electron/positron ($e^{\pm}$), it will produce a photon by *bremsstrahlung* ($e^{\pm} \rightarrow e^{\pm} + \gamma$), losing half its energy. The photon, in turn, splits its energy by pair production ($\gamma \rightarrow e^+ + e^-$). The $e^{\pm}$ should traverse a distance of $\lambda_e = X_0 \ln 2$
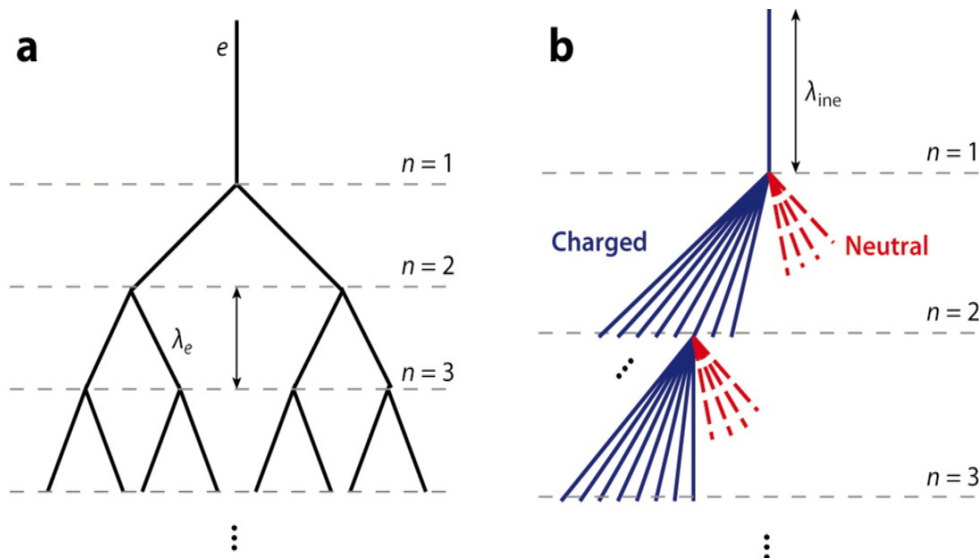
Figure 7 – The cascade toy models. *Left:* Heitler model, for electromagnetic cascades. *Right:* Heitler-Matthews model, for hadronic cascade.
Source: ENGEL; HECK; PIEROG. (51)

before any interaction, with X_0 being the radiation length of the medium ($\approx 37\,\mathrm{g\ cm^{-2}}$ for air). The photon has a mean free path in the same order of λ_e, and therefore, the model assumes a propagation of equal lengths for any of them.

The number of particles at a given depth $X = n \cdot \lambda_e$, is given by $N(X) = 2^n = e^{X/X_0}$, with n being the number of interactions, as depicted by the left of Figure 7. The energy of a particle after n interactions is then $E(X) = E_0/N = E_0 \cdot e^{-X/X_0}$. The cascade continues until ionization energy losses dominate over the production process, *i.e.* the $e^\pm$ energy falls below ϵ_{crit}^e, reaching a maximum number of particles N_{max}^{EM} at a depth of X_{max}^{EM}. For the air, this critical energy is $\epsilon_{crit}^e \approx 87$ MeV. (63) Working with the expressions for $N(X)$ and $E(X)$, the quantities N_{max}^{EM} and X_{max}^{EM} are given by

$$N_{max}^{EM}(E_0) = \frac{E_0}{\epsilon_{crit}^e} \tag{3.6}$$

and

$$X_{max}^{EM}(E_0) = X_0 \ln\left(\frac{E_0}{\epsilon_{crit}^e}\right) . \tag{3.7}$$

For not too small X, the number of electrons represents approximately two-thirds of total particles, as

$$N_{e,max}^{EM}(E_0) = \frac{2}{3}\frac{E_0}{\epsilon_{crit}^e} . \tag{3.8}$$

Despite being a simple approximation, the Heitler model gives a important relationship with primary energy to these two parameters, that, as described in the previous
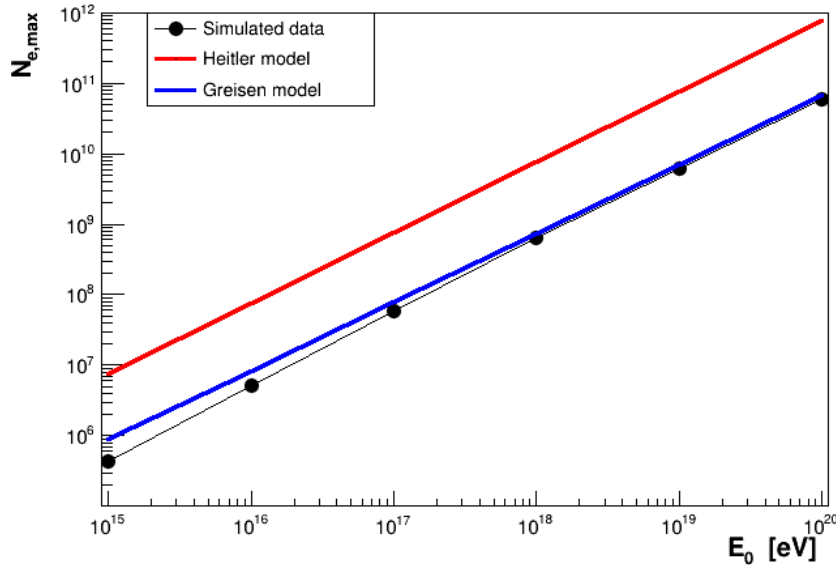
Figure 8 – Comparison between analytical results and simulated data by CONEX regarding average number of electrons at maximum.
Source: By the author.

section, are of a great importance for longitudinal profile reconstruction. The logarithmic relation between X_{max} and E_0 given by the model is in great accordance with Monte Carlo simulations. On the other hand, the linear relation for N_{max}^{EM} with E_0 is overestimated when compared to these simulations, giving a number greater by a factor of ~ 10, as can be seen in Figure 8, making the Heitler model not well suited for describing longitudinal profiles. Moreover, Heitler model does not account for the lateral distribution of electrons.

However, a more well suited description for the longitudinal profile for electromagnetic cascades can be given by the Greisen profile, (64) via its approximate solution to diffusion equations, giving the average number of electrons with energies greater than ϵ_{crit}^e

$$N_e^{EM}(E,t) = \frac{0.31}{\sqrt{\ln(E_0/\epsilon_{crit}^e)}} \exp\left[\frac{X}{X_0}\left(1 - \frac{3}{2}\ln s\right)\right], \tag{3.9}$$

with s being the shower age, presented in Equation 3.5. The quantity $N_{e,max}$ can then be calculated after taking the same steps for Equations 3.6 and 3.7, by

$$N_{e,max}^{EM}(E_0) = \frac{0.31}{\sqrt{\ln(E_0/\epsilon_{crit}^e)}}\left(\frac{E_0}{\epsilon_{crit}^e}\right). \tag{3.10}$$

Figure 8 shows the great agreement between Greisen profile and Monte Carlo simulations, especially at higher energies, making the number of electrons at shower maximum a good estimate of the primary energy.

3.4 Hadronic Cascade

Protons and nuclei interactions with atmospheric nuclei induce hadronic showers. Hadronic particle production, unlike electromagnetic particle production, cannot be treated from first principles in quantum field theory, therefore, one has to resort on approximate phenomenological models. Derived from Heitler model, the Heitler-Matthews model (65) also assumes a branching development, but with more branches, accounting for more particle production, as described in Section 3.1 of this chapter. See the right panel of Figure 7, for a depiction of this model.

A primary hadron with E_0 should produce N pions via interaction with atmospheric nuclei, each with energy E_0/n_{tot}, where exactly two-thirds are charged pions ($\pi^\pm$), and one-third should be neutral particles (π^0). π^0 immediately decay into a pair of photons ($\pi^0 \to 2\gamma$) thanks to its short lifetime ($c\tau = 25$ nm), generating a electromagnetic subshower. $\pi^\pm$ decay via $\pi^\pm \to \mu^\pm + \nu_\mu/\bar{\nu}_\mu$. Having greater lifetimes ($c\tau = 7.8$ m for $\pi^\pm$), these charged particles typically interact with atmospheric nuclei before decaying, if their energy is above some critical decay value ϵ_{dec}, when the interaction length (λ_{had}) is greater than the decay length. The average lateral distribution and longitudinal profile of a proton-induced shower with $E_0 = 10^{19}$ eV are shown in Figure 4.

As the number of pions greatly exceeds any other type of particle in hadron-hadron processes, (66) the electromagnetic subshower quickly grows. In each hadronic interaction, this subshower receive about one-third of E_0 via π^0 decay. After n interactions, the energies of the hadronic and the electromagnetic components should be, (51, 52) respectively,

$$E_{had} = \left(\frac{2}{3}\right)^n E_0 \quad \text{and} \quad E_{EM} = \left[1 - \left(\frac{2}{3}\right)^n\right] E_0 \,. \tag{3.11}$$

Since $n \geq 5$ for energies $\geq 10^{15}$ eV, (67) most of the energy is carried by the electromagnetic subshower.

A proton-induced cascade will have a maximum number of electrons at an atmospheric depth equal to the sum of depth of the first interaction, given by λ_p and X_{max}^{EM} of the electromagnetic subshower (Equation 3.7), accounting for photon pair production, modelled as

$$\langle X_{max}^p \rangle = \lambda_p + X_0 \ln\left(\frac{E_0}{2N\epsilon_{crit}^e}\right) \,. \tag{3.12}$$

However, multiplicity and interaction length vary with the logarithm of primary energy, and need to be accounted for. Defining B_N as the multiplicity change and B_λ as the interaction length change, for proton-induced showers,

$$B_N \equiv \frac{d\ln N}{d\ln E_0} \quad \text{and} \quad B_\lambda \equiv -\frac{\lambda_p}{X_0}\frac{d\ln \lambda_p}{d\ln E_0} \,, \tag{3.13}$$

changes in X_{max} by $\ln E_0$ are then given by

$$D_p = \frac{d\langle X_{max}^p \rangle}{d \ln E_0} \approx X_0(1 - B_N - B_\lambda) \,. \tag{3.14}$$

The quantity D_p is the *elongation rate* for proton-induced showers, a measure of the variation of shower maximum per logarithm of energy. In the general form, D is defined as (68, 69)

$$D = \frac{d\langle X_{max} \rangle}{d \ln E_0}. \tag{3.15}$$

Furthermore, hadronic interactions models predict $B_N, B_\lambda > 0$, giving, by Equation 3.14, the upper bound of X_0. These models also predict an approximately constant D_p and, therefore the average X_{max}^p is

$$\langle X_{max}^p \rangle = c + D_p \ln E_0 \tag{3.16}$$

with c and D_p given by hadronic interaction models. These results are Linsley's *elongation rate theorem*, a powerful tool for experimental analysis of X_{max}.

For estimate of particle number, again the toy models are useful. In Heitler-Matthews model, the hadronic cascade is initiated by a proton, in a depth of λ_{ine}, and is assumed to produce only pions via interactions with atmospheric nuclei, where exactly two-thirds are $\pi^\pm$, N_{ch}, and one-third are π^0, $N_{ch}/2$. Charged pions interact after traversing a depth of λ_{ine} where another interaction happens, producing each N_{ch} more charged pions and $N_{ch}/2$ more neutral pions. Neutral pions decay immediately. After n interactions, each atmospheric layer of depth λ_{ine} (refer to Figure 8) contains $N_\pi = (N_{ch})^n$ charged pions, with energy of $E_\pi = (2/3N_{ch})^n E_0$. These particles decay into muons after E_π is smaller than some critical decay value ϵ_d^π. The number of muons is then

$$N_\mu^p = \left(\frac{E_0}{\epsilon_d^\pi} \right)^\beta \,, \tag{3.17}$$

with $\beta = \ln N_{ch} / \ln N$, predicted to be in the range of 0.88 to 0.92 [70] by air shower simulation.

The number of electrons at shower maximum for proton-induced showers is estimated from the total amount of energy in the subshower minus the muon component energy. At high energies, it can be approximated to simply (52)

$$N_{e,max}^p \approx \frac{E_0}{\epsilon_{crit}^e} \,, \tag{3.18}$$

given that the energy fraction transferred to muons becomes negligible.

The quantities above discussed can be generalized to the case of nuclei-induced showers, using the superposition model. When accounting that EAS are originated by

high-energy particles, the binding energy of nucleons is negligible compared to the primary particle energy (~ 5 MeV $\ll 1$ EeV). Based on that, the superposition model says that a primary nucleus of mass A and energy E_0 can be treated as a superposition of A nucleons of energy $E' = E_0/A$. (52) Of course the model is limited, *i.e.* it does not account for nuclear effects, such as nuclear fragmentation, but it can provide a qualitative description of the basic physics phenomena behind a observable. For instance, the number of muons can be estimated by making $E_0 \to E_0/A$ and adding a factor of A in Equation 3.17 (52,65)

$$N_\mu^A = A \left(\frac{E/A}{\epsilon_d^\pi} \right)^\beta = N_\mu^p A^{1-\beta} \,. \tag{3.19}$$

Similarly, the number of electrons at maximum shower for nuclei-induced shower

$$N_{e,max}^A = A \frac{E/A}{\epsilon_{crit}^e} = N_{e,max}^p \,. \tag{3.20}$$

These two results provide good estimates of primary mass composition, by muon number, an primary energy, by electron number, independent of composition. Moreover, average X_{max} for nuclei-induced shower can also be estimated with the superposition model by adjusting Equation 3.16 via $\langle X_{max}^A \rangle = c + D_p \ln(E_0/A)$. However, X_{max} is not an additive property, unlike particles number, and for each subshower, the average X_{max} is expected to be

$$\langle X_{max} \rangle = c + D_p \ln(E_0/A) = \langle X_{max}^p \rangle - D_p \langle \ln A \rangle \,, \tag{3.21}$$

assuming the primary flux to have an average logarithmic mass $\langle \ln A \rangle$, implying that heavy primaries reach shower maximum at smaller depths than light ones. (52)

3.5   Air Shower Simulation

Given that Extensive Air Showers data are extremely rare (refer to Chapter 2) and the observed data is subject to missing values, fluctuations and uncertainties, computer simulations provide the only complete data for EAS study. Real data can provide relations with different primaries, and these can be used in simulations. In addition to EAS rarity, this work will focus on the exotic Q-ball as primary particle for an EAS — which has never been seen in real data. So, in order to proceed with the study, computer simulation is the essential tool.

Regarding the available algorithms for the purpose of EAS simulation, CONEX (71) and CORSIKA (72) are of common choice. The latter uses the full Monte Carlo approach for full descriptions of EAS, but requires a huge execution time for Q-ball simulation. (73) The former, on the other hand, uses a one-dimensional hybrid approach: (74) full Monte Carlo, for the early high energy interactions, combined with fast numerical solution of cascade equation, for the resulting secondary particles.

Conex's Monte Carlo method is very similar to Corsika's, but in one-dimensional — that is, only particle movement along shower axis are considered. For the numerical solution, the boundaries conditions in the cascade equations are set as particles with energies below 0.5% of the primary particle energy. (71) This one-dimensional equation solution provides a fast simulation, thanks for the fact that after few interactions, the secondary particle energies fall mostly below this fraction. (33, 75) The equation aims to solve a set of functions, each for each particle type, within an energy range located at an interval of atmospheric depth. The transition rate between particle type is tabulated following the interaction model used in Corsika), for discrete energy interval. Conex) provides good estimates for the observables. (71)

The down side for Conex simulation is that it provides only longitudinal profile observables (hence the one-dimensional description), but this will be proved enough for the purposes of this work. The observables X_{max} and dE/dX, that is, the energy deposit of the EAS, will be well-suited for Q-ball profile analysis and cross-section parametrization (see Chapter 6), hence, there is no use for lateral distribution for this work. With that said, Conex was the obvious choice for this project.

4 THE PIERRE AUGER OBSERVATORY

Since the observations of UHECR reported in Linsley's work in 1963, the instrumentation for the study of UHECR has been improved and grown larger. The two main methods used now are surface arrays and the fluorescence telescopes — each one with its advantages and disadvantages.

Surface arrays can work under most atmospheric conditions. They have a simple but durable design and can run continuously, giving an almost 100% duty cycle and can provide most of the statistical data for cosmic ray study. However, they strongly depend on calibration or models and provide limited information for singular events. Fluorescence telescopes, in contrast, are much more used for large information about each shower, but they can only operate in clear moonless nights, giving then a duty cycle of about 15%, with variations given by the delicacy of the instrument, further reducing its duty cycle.

Being a hydrib detector, the Pierre Auger Observatory should surpass the weakness of each observational method — it is able to measure both the lateral (by the surface array) and longitudinal profile (by the fluorescence telescope). Commissioned in 2008, but taking data since 2004 (76), it is located in Malargüe, Argentina, and it is the result of a world-wide collaboration, with more than 400 scientists from 17 countries around the globe working on it. Figure 9 presents the Pierre Auger Observatory layout: 1660 ground-based water-Cherenkov detectors, the Surface Detector (SD), and the 27 fluorescence telescopes split into 4 detector sites, the Fluorescence Detector (FD), covering an area of over 3000 km^2. Three laser facilities for atmospheric monitoring and the radio detectors AERA system are also part of the Pierre Auger Observatory layout, being located inside the array. When counting its calorimeter, the atmosphere above it, it is the worlds largest detector as it is the largest cosmic-ray experiment. (22) The Pierre Auger Observatory was designed to the study of UHECR, working primarily in the high energy end of the of the energy spectrum (see Chapter 2); 10^{19} to 10^{21} eV. Also, it counts with a robust package for cosmic rays analysis, the $\overline{\text{Off}\underline{\text{line}}}$, (77) a framework built for reconstruct and simulate data for the Pierre Auger Observatory.

4.1 The Surface Detector

Spaced in a 1.5 km triangular grid, the water-Cherenkov surface detectors are the heart of the observatory. In addition to the main array, a smaller one — called the *infill* array —, covering 23.5 km of area is formed by 60 detector, with half the separation of the main one, as seen in the field of view of the HEAT in Figure 9. The *infill* array is designed to measure low energy events, extending the energy range to 10^{17} and 10^{18} eV. (79, 80)
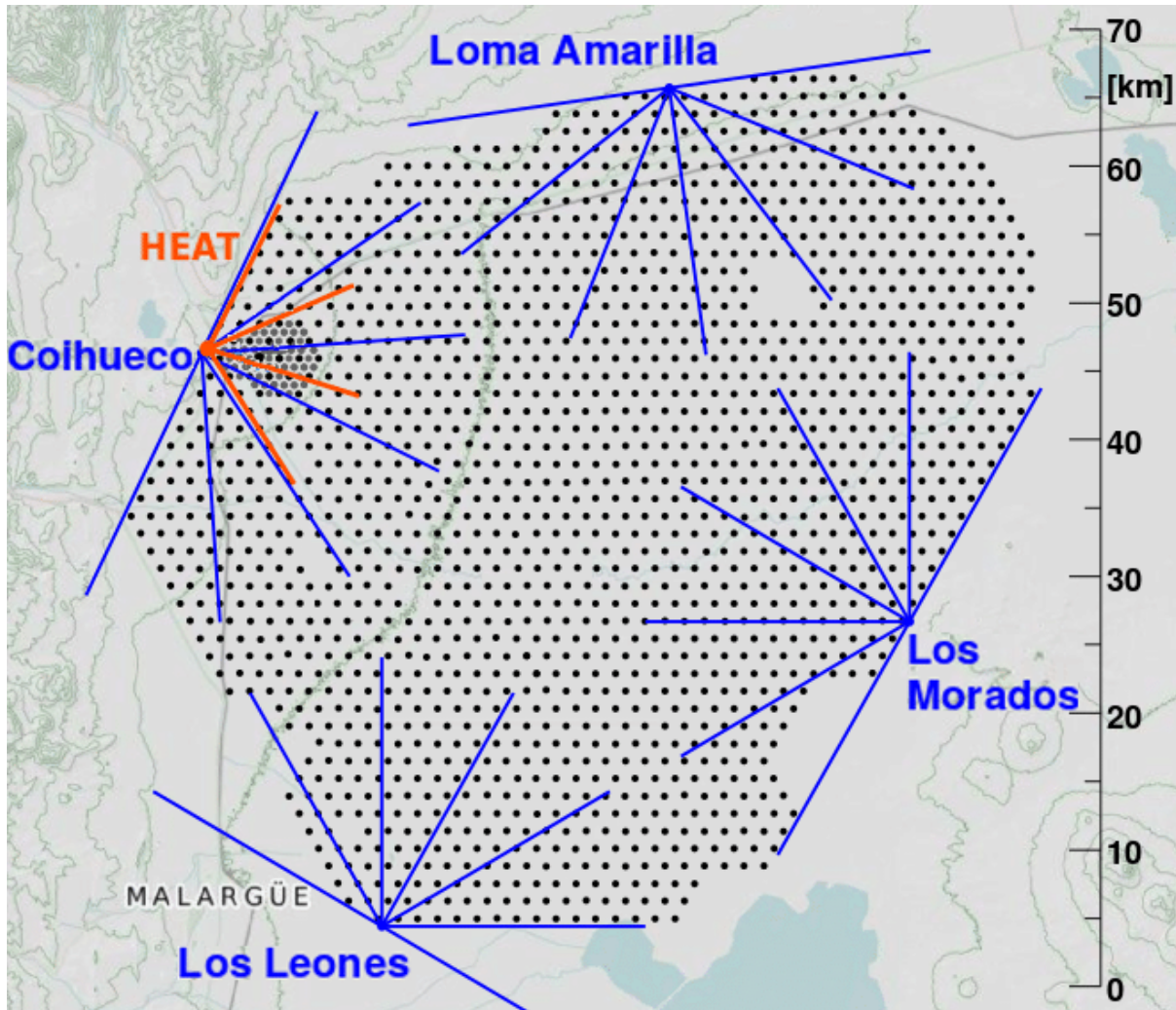
Figure 9 – The Pierre Auger Observatory: dots represent the surface detector stations, with the condensed group representing the *infill* array, and the blue lines delimit the field of view of the six fluorescence detectors at each of the four detector sites Los Leones, Coihueco, Loma Amarilla and Los Morados. The High Elevation Auger Telescopes (HEAT) field of view are shown in red lines. The three atmospheric monitoring laser facilities and the Auger Engineering Radio Array (AERA) are not shown.
Source: GORA *et al.* (78)

Each detector is a self-sufficient solar-powered cylindrical tank that operates autonomously. It is composed of polyethylene and has dimensions of 3.6 and 1.2 m, in diameter and height, respectively. A GPS clock is used for precise event timing and a radio broadcast antenna for communication with the Central Data-Acquisition System (CDAS). Inside the tank, 12 m³ of ultra-pure water is encased by a highly internally reflective and opaque Tyvek© bag, and three photomultiplier tubes (PMT) are symmetrically placed in the upper surface of the tank to collect Cherenkov light data from shower particles. A scheme of a detector and its data acquisition is presented in Figure 10. The water can be
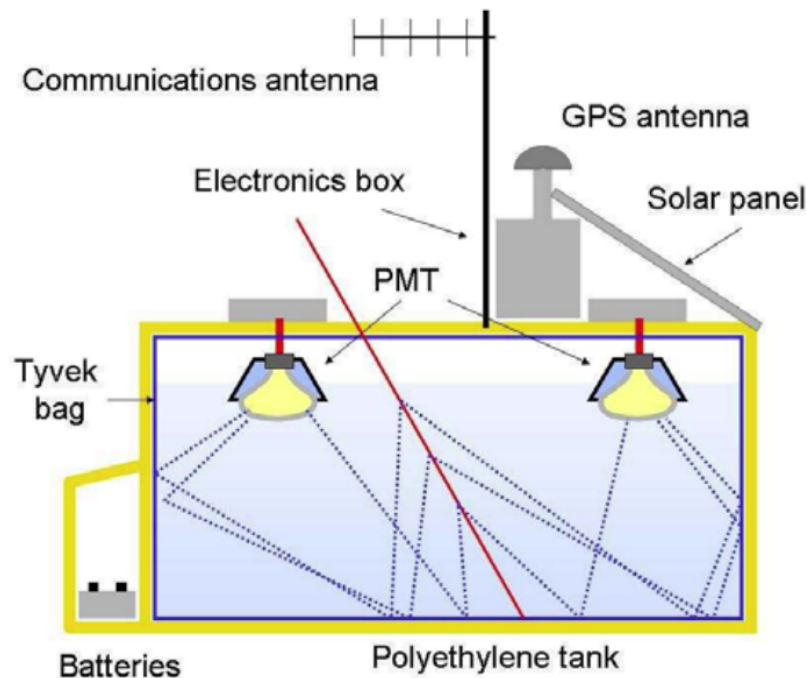
Figure 10 – Schematic view of the water-Cherenkov detector with its components and data acquisition. The dark red line represents a shower particle crossing the tank, with its Cherenkov light, the blue dashed lines, produced by its passage through water being reflected in the walls of the highly reflective encasing and reaching the photomultiplier tubes (PMT).
Source: SHELLARD.(82)

considered optically isolated and in almost total darkness. This, combined by the durable tank, makes the SD reliable and able to work over continuously time and through a variety of weather conditions. (81)

The acquisition chain for a event detected by the SD follows a five-level trigger system. The first two triggers, T1 and T2 are single-station. They are calibrated based on the charge collected by a PMT from the Cherenkov light produced by a muon vertically entering tank; "Vertical Equivalent Muons" (VEM). A peak in the distributions of charge and pulse height, Q_{VEM}^{peak} and I_{VEM}^{peak} respectively, are produced by atmospheric muons and are measured proportionally to those produced by a VEM.

T1 is divided in a Time-over-Threshold trigger (ToT) and a simple Threshold trigger (TH). If the three PMTs measure a signal of 1.75 I_{VEM}^{peak} or more, the TH is passed, and if the signal exceeds 3.2 I_{VEM}^{peak}, it is promoted to a stricter form of T1-TH, the T2-TH. T1-ToT requires that at least two of the three PMTs measure a 0.2 I_{VEM}^{peak} within 3 μs, and after the trigger is passed, it advances to T2-ToT. The ToT rate is of 2 Hz for both T1 and T2, and the TH rate is 100 Hz for T1, and 20 Hz for T2. The T2 triggers are sent to the CDAS where they are examined for spatial and temporal correlation with other stations signals, forming an array trigger (T3).
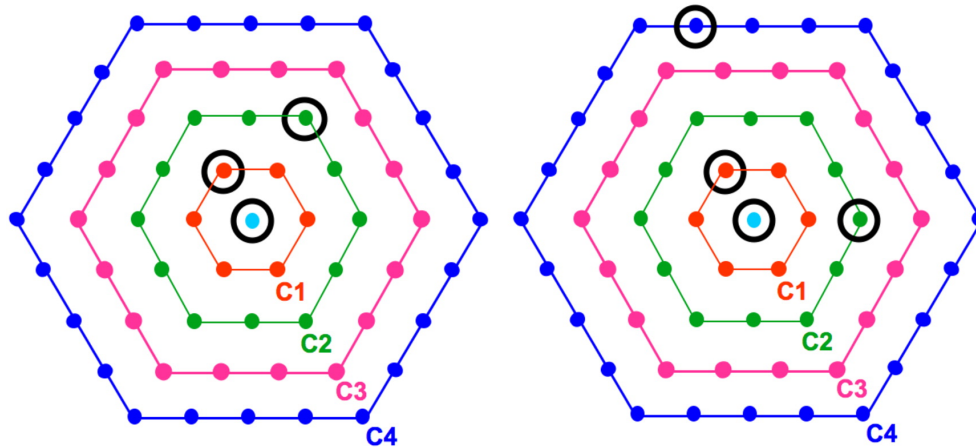
Figure 11 – Example of T3 spacial configuration. *Left:* T3 first mode. *Right:* T3 second mode. C1 to C4 indicate the first to fourth sets of neighbours, respectively. Source: ABRAHAM *et al.* (83)

T3 looks for coincident signals in the SD and/or the FD. The trigger of the array is done in two modes. The first mode of T3 requires three T2-ToT stations in a compact shape (left of Figure 11) and within a time window of $(6 + 5C_n)\,\mu$s, where C_n indicates the nth set of neighbours (see Figure 11). This mode has a rate about 0.02 Hz. The second mode is less restrictive requiring four fired T2 with the same time window as the first mode (right of Figure 11). Past the T3 array, the data is sent to the T4 trigger. If, however, the T2-station is isolated, but the FD also triggered during the SD event (see Section 4.2), then the FD's T3 trigger evaluates the significance of the signal from the SD station. If it passes the FD's T3 trigger, the signal is stored as a hybrid event.

T4, the physics trigger, is responsible for select real air showers from T3 data and starts the event selection for reconstruction. It is also divided in two criteria: The 3ToT and 4C1. 3ToT requires three nearby ToT-T2 stations in a triangular pattern and a signal time fit to a plane shower front moving at the speed of light. This requirement gives a rate also about 0.02 Hz. The second criteria, 4C1 requires four nearby stations of T2 stations, with the same time fit of 3ToT criterion. This reduces its rate, being about 1×10^{-3} Hz, but ensures a physically realizable shower. Passing any of the criteria, the signal is sent to the T5 and last trigger.

The final trigger level, T5, it is only necessary for events that fall close to the edge of the array. To pass it, a central hot tank is selected, the one with the highest signal at the time of the event, with all its C1 neighbours also triggered.

This acquisition chain of the SD gives a efficiency of about 99% for air showers with energy greater than 3×10^{18} eV, and reduces the counting rate of single stations to $\sim 3 \times 10^{-5}$ Hz. This gives a rate of events of $\sim 5 \times 10^{-2}$ Hz for the entire array, being almost all due to EAS. (83, 84) A representation of such event is presented in Figure 12.
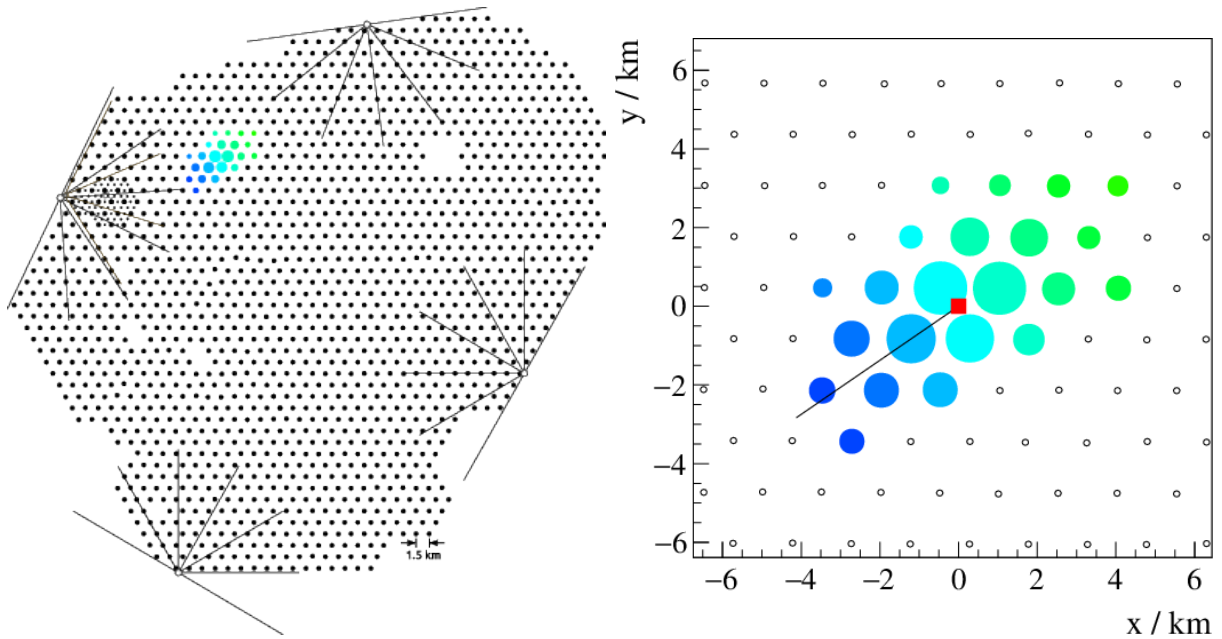
Figure 12 – Example of a shower event measured by the surface detector, reconstructed with $\theta = 55.2°$ and energy of $38.7\,EeV$. *Left:* the Pierre Auger Observatory layout, with dots representing the surface detector and lines representing the fluorescence detector. The colored dots correspond to those stations that participate in the measurement. *Rigth:* zoomed-in view of the event. The black line represents the sower axis on the ground, and the red square represents the impact point of the shower-core. The SD stations colors represent the trigger time (blue is early, green is late), with their area proportional to the logarithm of the signal.
Source: AAB *et al.* (84)

4.2 The Fluorescence Detector

Overlooking the SD array, the Fluorescence Detector consists of four elevated stations (Eyes), each one with six telescopes, plus a smaller and additional one, the High Elevation Auger Telescopes (HEAT), with three telescopes developed for low energy measurements along with the *infill* array, as presented in Figure 9 and Section 4.1. The blue lines in Figure 9 represent the field of view (FOV) of the telescopes, each one with a $30° \times 30°$ in azimuth and elevation, giving each Eye a total of $180°$ in azimuth and a maximum in $30°$ in elevation. This allows the Fluorescence Detector to measure longitudinal profiles from about 200 to $1800\,m$, usually. The red lines represent the FOV of the HEAT, each with a $30°$ to $58°$ observing elevation angle. (80, 85)

As seen in Figure 13, the telescope is composed of a shutter, only opened when appropriate data acquisition condition is met or for maintenance, an aperture system, that contains a filter and corrector lens, segmented mirrors, a PMT camera and electronics. The filter absorbs visible light while transmits UltraViolet (UV) one, from ~ 290 to
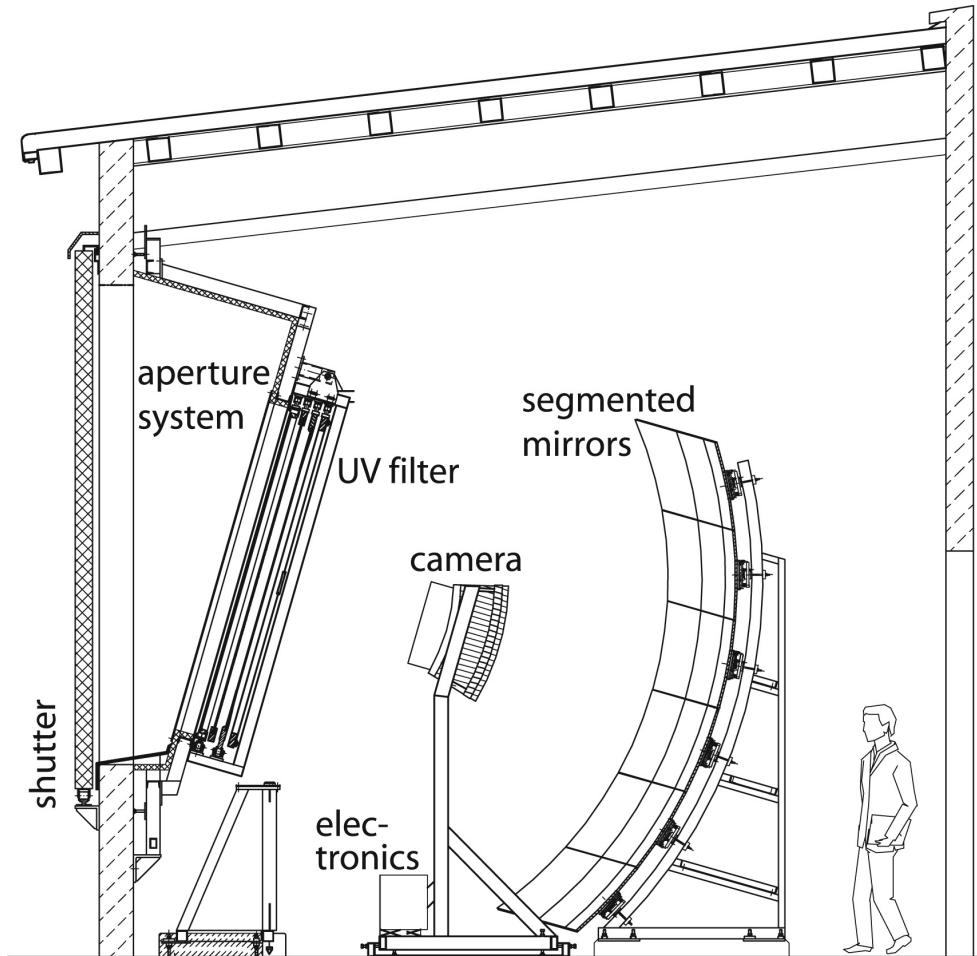
Figure 13 – Schematic view of a fluorescence telescope of the Fluorescence Detector, with its main components described.
Source: ABRAHAM *et al.* (85)

~ 410 nm wavelength photons, that includes almost all of the atmospheric nitrogen fluorescence spectrum. The camera is composed by 440 PMTs in a hexagonal grid and is controlled by a robust and sophisticate trigger system, registering possible showers with a 100 ns resolution for photon counting based on time signal evolution in tracks of triggered pixels. The segmented mirrors reflect light towards the camera and has two configurations, covering about 13 m^2 of area each; 60 segmented hexagonal glass mirrors or 36 segmented rectangular anodized aluminum mirrors. The whole apparatus is remotely controlled, and requires a monitoring of atmospheric conditions both for calibration and data acquisition. It also has a communication antennae, for contact with CDAS, a clock module and a GPS system for event timing and position. (85)

The FD is calibrated for the isotropically fluorescence of atmospheric nitrogen's valence electrons for record, timing, intensity and evolution measurements. This UV light can easily be lost in atmospheric background light, making the FD only operable in moonless, cloudless, clear and dark skies, severely reducing its statistical data and duty
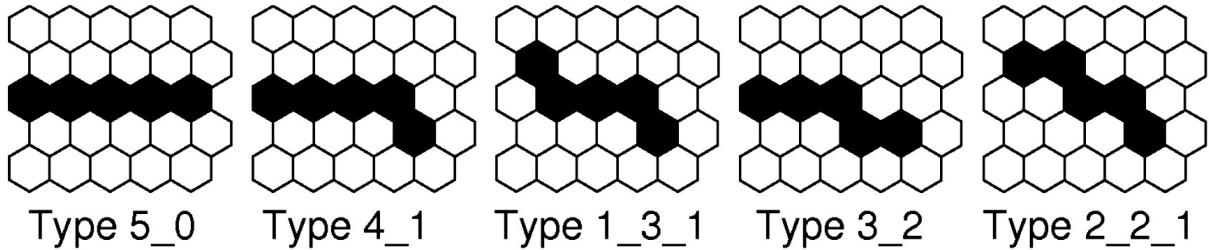
Figure 14 – Basic pattern types regarded as straight track segments for the Second Level Trigger of the Fluorescence Detector.
Source: ABRAHAM *et al.* (85)

cycle to about $\sim 14\%$. (85)

Like the SD acquisition-chain, the FD has a trigger system, each one more sophisticated than the previous. The First Level Trigger (FLT) is a threshold filter. It works with individual pixels in the camera and requires a integrated signal over 10 consecutive time bins (10×100 ns) for all triggered pixels to be above the adjustable threshold. The latter is dynamically set to ensure an FLT trigger rate of 100 Hz per pixel. When the integrated signal exceeds the threshold, the signal advances for the Second Level Trigger (SLT).

The geometric trigger, the SLT, looks for geometric patterns as show in Figure 14. It requires that in all PMT signals one of the total of 108 patterns originated from the track segments shown in Figure 14 is presented within a $20\,\mu$s time window, reducing the trigger rate down to 1 Hz per mirror. Once the SLT is passed, the data is sent for noise and random triggered events removing by the last station trigger.

The software algorithm designed Third Level Trigger (TLT) is responsible for cleaning up the signals from noise events, especially lighting signals and muon impact on camera. Firstly, a multiplicity trigger cuts off large background events by checking pixel timing. Based on background noise and several thousand true showers collected over one year, 1000 multiplicity values are compared to the event one, removing any event that is too bright for too long or that triggered more than 25 pixels — common lightning signal. Next, the remaining smaller events, that could correspond to muon impacts and random triggers, are filtered by a correlation between spatial arrangement and peak signal times of the triggered pixels. The algorithm is dynamic to atmospheric conditions, and reject less than 0.7% of true showers. (85)

After this trigger system is passed, the surviving events are sent to the EyePC within the station, where they are evaluated by the hybrid array trigger, the T3 that looks for correlated measurements in the SD. A fast and rough event reconstruction is performed by the EyePC to determine the shower's core location and timing in the SD array and sent to the CDAS to be compared with actual signals measured by the SD.

Correlated measured events in the FD and SD are then labelled hybrid events, being the most accurate data measured by the PAO. Since the SD has a 100% duty cycle, most of the FD recorded events are hybrid events.

4.3   Event Reconstruction

The PAO is a hybrid detector, an important aspect that gives the best results in geometrical accuracy and reduced uncertainties when timing information from both the SD stations and the FD pixels are used for event reconstruction. The individual event reconstruction will be presented for both the SD and the FD, as the hybrid event reconstruction is just another step in the FD event reconstruction.

The reconstruction of events for the SD — shower geometry, size and primary energy — is done using timing and signal size from the coincident triggered stations. First, using timing information, the shower geometry is reconstructed by using the start time of the signal t_i in each triggered station i in the $\vec{x}_i$ to fit the expected values $t_{sh}(\vec{x}_i)$ from a shower front moving at light-speed

$$\chi^2 = \sum_i \frac{[t_i - t_{sh}(\vec{x}_i)]^2}{\sigma_{t_i}^2} \,, \tag{4.1}$$

where σ_{t_i} is the uncertainty of t_i. The SD reconstruction has two frameworks based in the shape of the shower front: the *Herald* framework, where the front is considered with a constant curvature, and the *Observer* framework, with the front shape corresponding to a inflating sphere with a fixed origin point. The reconstruction is done independently is both of the frameworks, allowing for cross-validation. (84)

For the shower size reconstruction, a lateral distribution function (LDF), $S(r)$, is fitted to the signal of triggered stations in the SD, with r being the perpendicular distance to the shower axis. Briefly speaking, $S(r)$ has a general form of

$$S(r) = S(1000) \cdot f_{LDF}(r) \,, \tag{4.2}$$

with $f_{LDF}(r)$ being a data-derived average, scaled LDF shape fitted by station signals of individual events and $S(1000)$ is the shower-size estimator, corresponding to $r = 1$ km, chosen to minimize shower-to-shower fluctuations specifically for the SD triangular grid of 1500 m, (84) and to normalize $f_{LDF}(1000) \equiv 1$. Each framework has its own $f_{LDF}(r)$, which is parameterized in terms of $S(1000)$ and zenith angle θ of the shower axis. To get the position of the shower core $\vec{x}_c$ and $S(1000)$, a log-likelihood is maximized, given the product of probabilities P over $\vec{x}_c$, $S(1000)$ and the observed signal sizes S_i in the stations at $\vec{x}_i$

$$\ln \mathcal{L} = \sum_i \ln P(S(1000), \vec{x}_c \mid S_i, \vec{x}_i) \,, \tag{4.3}$$

with both frameworks having its model to calculate P. (84)

In order to obtain the angular accuracy of the events reconstruction, two arrival directions are compared based on the shower front arrival time at each station — that is a function of number of particles, their time distribution in the front and the area of the stations —. Usually, one of the arrival direction is a simulated reconstruction, and the other is the real one. However, the directions can also be both reconstructed by the same procedure or each one be the result of different methods. This procedure is also done in both of the frameworks independently, providing an angular resolution better than 1.4°, improving with a increase in energy and zenith angle. (84)

Finally, the primary energy estimation for the SD begins with the shower size reconstruction. The measured $S(1000)$ is converted to S_{38} by the constant intensity cut (CIC) method*, (28) that is equivalently the size of a shower with a primary particle arriving with $\theta = 38°$, that is a median value, that $S_{38} = S(1000)/f_{(CIC)}(\theta)$, with $f_{(CIC)}(38°) \equiv 1$. The minimally biased and zenith-independent energy estimator S_{38} is then calibrated by the energy reconstructed by the FD using hybrid events — that are reconstructed both by the FD and SD. The calibration curve is described by the power law $E = A(S_{38}/\mathrm{VEM})^B$, which is used to estimate the energy of all SD events, giving an uncertainty of about 14%. (28, 84)

The FD is able to reconstruct the longitudinal development of a shower by a two-step event reconstruction from the registered tracks (Figure 15, left); geometry and calorimetric energy-deposit profile.

First, for the geometric reconstruction, it is necessary to determine the shower-detector plane (SDP), the plane that includes almost all of the FD pixels centered on the shower axis through the Eye. Straight forward, it is the plane that includes both the Eye location and the shower axis' line, as shown in Figure 16. The shower is assumed to be a point-like source of isotropic light moving with light-speed at a perpendicular distance R_p from the telescope to the shower axis, with an angle χ_0 between the horizontal line in the SDP and the shower axis. For each i-th pixel that observes the track, a point direction is measured, the viewing angle χ_i. The arrival time of photons at the i-th triggered pixel is then

$$ t_i = t_0 + \frac{R_p}{c} \tan\left(\frac{\chi_0 - \chi_i}{2}\right), \tag{4.4} $$

where t_0 is the time when the shower front passes through R_p on the axis. The shower parameters are determined by data fitting and completely specify the shower axis, giving an angular resolution of 0.6°. (85)

---

* This method considers the electromagnetic cascade attenuation by the increase in atmospheric depth. The attenuation factor $f_{CIC}(\theta)$ is empirically derived. Detailed description can be found in (28).
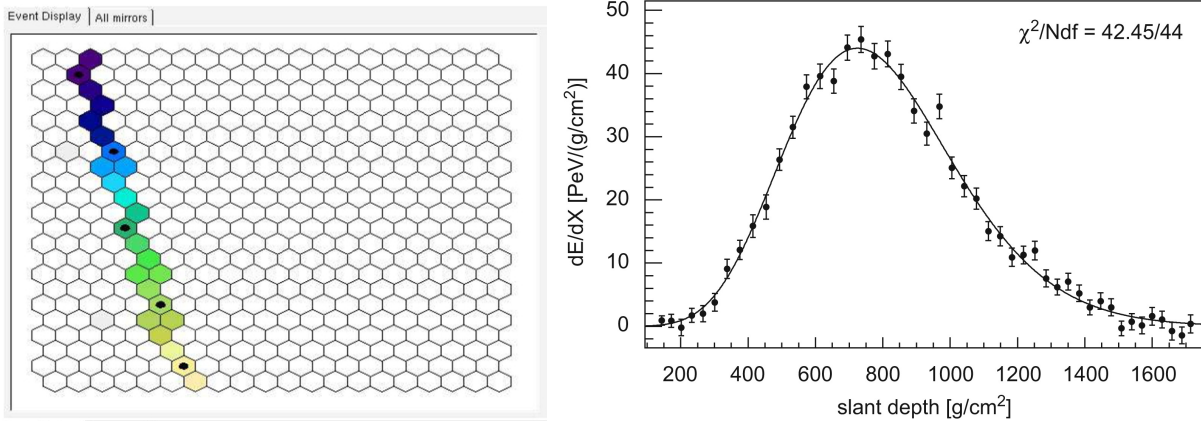
Figure 15 – Examples of shower track and longitudinal profile reconstructed. *Left:* A cosmic ray shower event pattern of activated pixels (blue is early, light-yellow is later). *Right:* energy deposit profile reconstructed. Dots are the reconstructed data and the line is the fitted Gaisser-Hillas function.
Source: Adapted from ABRAHAM *et al.* (85)
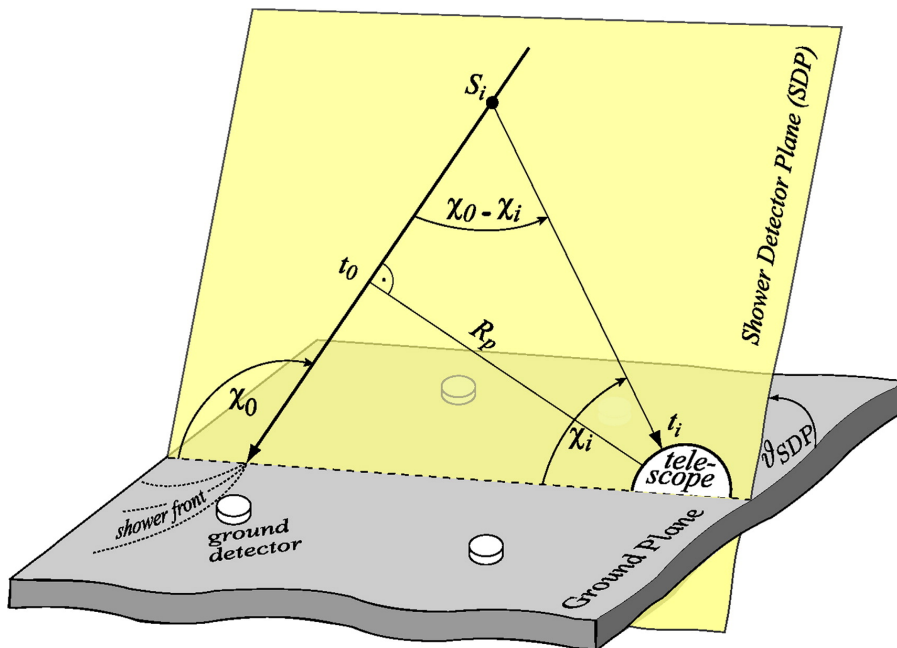
Figure 16 – Shower detector plane illustration and geometrical shower reconstruction of a Extensive Air Shower from the observables of the Fluorescence Detector.
Source: KUEMPEL; KAMPERT; RISSE. (86)

After the geometry of the shower is reconstructed in the FD, the deposit of energy reconstruction begins with a disentanglement of the light signal received in the aperture. The light signal is the sum of three contributions: direct fluorescence light, direct and scattered Cherenkov light and multiple-scattered light. (85) This collected light at time t_i is then converted to energy deposit as a function of slant depth and thus the longitudinal profile $(dE/dX)_{cal}$ is plotted (black dots in Figure 15, right).
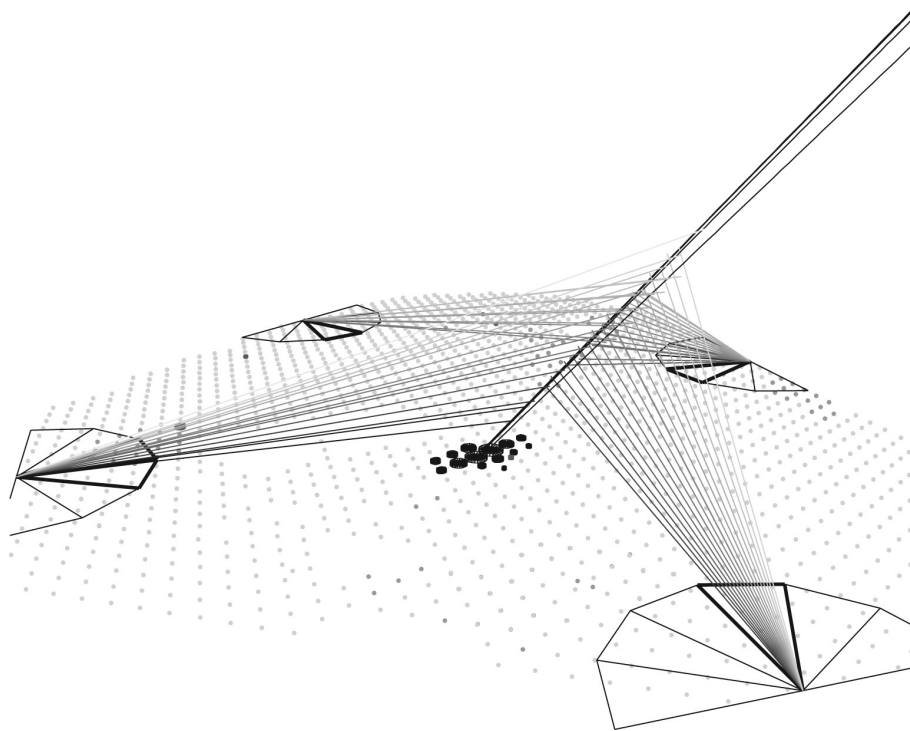
Figure 17 – Illustration of a hybrid event reconstruction.
Source: PIERRE AUGER COLLABORATION. (22)

The calorimetric energy is estimated by the integral of the fitted Gaisser-Hillas function (56) on the reconstructed energy deposit. The GH function for energy deposit rate has the form

$$\left(\frac{dE}{dX}\right)_{cal} = \left(\frac{dE}{dX}\right)_{max} \left(\frac{X - X_0}{X_{max} - X_0}\right)^{\frac{X_{max} - X_0}{\lambda}} \exp\left(\frac{X_{max} - X}{\lambda}\right), \qquad (4.5)$$

where X_{max} is the slant depth at which the shower reaches its maximum energy deposit rate, $(dE/dX)_{max}$, and the two fit parameters relates to shape. The primary composition and energy related X_0 is a virtual starting point of the shower development, and λ, relates to shower width (see Equation 3.3 for the Gaisser-Hillas function that relates number of particles in the shower and slant depth). At last, for primary energy estimation E_0, a correction is performed by taking into account an "invisible" energy lost ϵ_{inv}, that relates to the weakly interacting neutrinos and muons produced in the shower, that is invisible to the FD, via

$$E_0 = E_{cal}(1 - \epsilon_{inv})^{-1}. \qquad (4.6)$$

In the PAO, ϵ_{inv} is derived via a data-driven method described in (87). The hybrid reconstruction is simply the reconstruction done by the FD, called monocular reconstruction, with the added timing and location signals of the SD hot-tank. This added information requires parameter adjustment. The three free parameters in equation 4.4

must be corrected by the minimum of the function

$$\chi^2 = \sum_i \frac{(t_i - t(\chi_i))^2}{\sigma(t_i)^2} + \frac{(t_{SD} - t(\chi_{SD}))^2}{\sigma(t_{SD})^2}. \qquad (4.7)$$

This equation runs over all triggered pixels as well the SD triggered stations. The σ values correspond to the uncertainties for timing in the triggered pixel and the SD station. t_{SD} and χ_{SD} are the signal start time in the hot tank and the angle formed by the shower front containing the hot tank and the shower axis. An example of hybrid event, observed by the fours Eyes and the SD array is shown in Figure 17. The black lines represent the individual reconstruction for each Eye based on hybrid reconstruction.

A single hot tank data from the SD can reduce core position error of a shower significantly, and SD-FD merged data gives a lower energy threshold for the initial PAO design; from about 10^{19} eV to below 10^{18} eV.

4.4 The $\overline{\text{Off}\underline{\text{line}}}$ Framework

Created to provide a strong tool-set for reconstruction and simulation of air shower events and ensure a standardization between results for a collaboration that is globally spread, the $\overline{\text{Off}\underline{\text{line}}}$ is a robust customizable C++ framework that is the central backbone of Pierre Auger Observatory analysis, reconstruction and simulation work done by the collaboration. The $\overline{\text{Off}\underline{\text{line}}}$, as shown in Figure 18, has three main components: the detector description, the analysis modules algorithms and the event data. (77)

The detector description is a gateway for all the needed data to describe the configuration of the observatory when measuring and recording an event. This includes the nature of the detector, performance and atmospheric and environment conditions. This is for both real events or simulated ideal ones, or a combination of both. This allows the user to create unique scenarios and to test the observatory capability of reconstructing extreme events. Since all modules can be tweaked and the detector description can be changed, many scenarios of data can be created and studied.

The analysis modules are comprised by a collection of processing algorithms that can be modified and each one is dedicated for a specific task for the data analysis. The modules can be sequenced through instructions given in a XML file called Module Sequence and have its settings specified in the Bootstrap XML file. The data to be read is pointed in the Event File Reader XML, and each module is isolated from the others, allowing specific changes for specific modules. In the default configuration of $\overline{\text{Off}\underline{\text{line}}}$, one can readily simulate, reconstruct and analyse an event for the Pierre Auger Observatory.

Finally, the event data contains all type of data needed for the analysis modules. Calibrated or raw, reconstructed or Monte Carlo data, the event data structure provides it all and acts as a communicator between modules. For a real data, the event data first
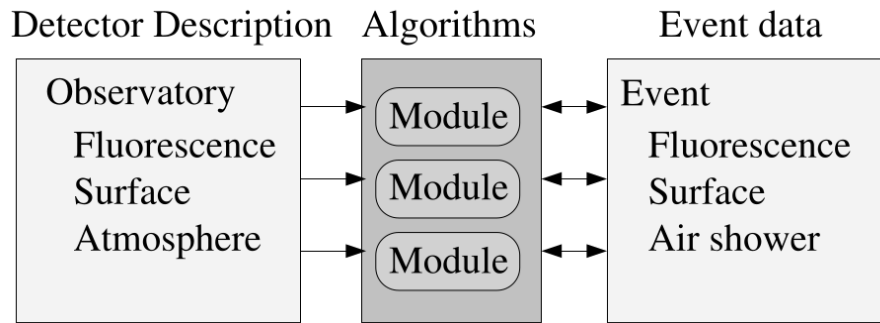
Figure 18 – General structure of the $\overline{\text{Off}}\underline{\text{line}}$ Framework. Both data simulation and reconstruction are done within modules. Each module reads data from the detector description and/or the event, performs its analysis and updates the data information to event data for the next module.
Source: ARGIRO *et al.* (77)

acquire the detector response, and after feeding this data for the analysis modules, it stores the response from them, the reconstructed data. For a simulation, the event data is filled after an event builder module feeds it with a simulated detector response data, starting then the same process of real data.

Along with this general structure, the $\overline{\text{Off}}\underline{\text{line}}$ also has visualization, plotting and geometry packages, a MySQL database handler and the tool-set from Cern's ROOT framework, (88) allowing with ease data importation and exportation, storage, interpretation and simulation. (77)

The Pierre Auger Observatory was designed to study UHECR, up to the extreme high-end of the energy spectrum. The capability of reconstruct shower events and even primary energy estimation with high accuracy provides a great step forward towards a better understanding of the mysteries from UHECR. Nevertheless, their nature and origin still without final answers. As human kind reaches these extreme environments, what one could possibly hope to find? Are we getting close to new physics? Air shower phenomenology and the observables from its detection and UHECR are still limited by our technology and capability of interpretation, leaving us still unsure about what lies beyond in this field.

5 Q-BALLS

The center-of-mass collision energies of UHECRs and particles in the atmosphere fall, by a factor of ~ 30, above the limits of human-made accelerators. (89 - 90) For that reason, UHECRs data may provide unique samples of new physics that is almost at reach of human kind. The origins and sources of UHECRs are still active areas of study, and one possible candidate for them are exotic particles $(44, 91\text{–}93)$ — hereafter, air showers initiated by exotic particles will be called exotic air showers. Within these exotic particles, there is a very stable hypothesized supersymmetric particle that, despite being a candidate for cold dark matter, strongly interacts with matter: the Q-ball. $(91, 94\text{–}96)$

5.1 Q-balls Properties

Predicted by Minimally Supersymmetric extensions of the Standard Model (MSSM) theory, the Q-ball was first theorized by Coleman, in 1985 (97) as a non-topological soliton after the pioneer work, in 1976, of Friedberg, Lee and Sirlin in solitons [98] which are single wave functions of supersymmetric quarks (squarks), or supersymmetric leptons (sleptons) that forms a Bose-Einstein condensate. But what is a soliton and why is it non-topological? A soliton is a solution that appears in quantum field theory, being non-linear and non-dissipative. If the soliton has a conserved Noether charge, it is said to be a non-topological soliton (otherwise, if it has a conserved topological charge, it is a topological soliton). For further readings in solitons, see. (98 - 99).

Q-balls are theorized to have been produced in a large number during the baryogenesis according to most supersymmetric theories and to be absolutely stable. (73) Their stability is due to the conservation of a global U(1) charge, or quantum number. Coleman called this type of matter as Q-ball, since Q plays the role of the quantum number to be conserved. Q is played by the baryon number, Q_B (or lepton number, Q_L for sleptonic Q-balls) and, after a certain baryon number threshold is reached, they should become stable $(94, 96, 100)$ - this should make them present in the universe to this day. There are two hypothesized types of Q-balls: neutral (Supersymmetric Electrically Neutral Solitons - SENS) and charged (Supersymmetric Electrically Charged Solitons - SECS). The interaction models and detection aspects drastically change based on the Q-ball type. $(91, 100)$ This work will be focused on the neutral type of Q-ball, SENS, as SECS should be easier to detect with our current technology (100) and most of the work present in literature treats about then. The interaction model of Q-balls during the development of air showers, which will be described below, is already implemented in CONEX), by the valuable work of Dr. Schuster and Dr. Pierog. (101)

5.2 Interaction Model

For SENS, there is no Coulomb barrier to prevent protons to access the interior of the Q-ball in collisions. The proton will be able to violate both Q_B and Q_L, but preserving the quantity $Q_B - Q_L$, as pointed out by. (73) This will trigger a process analogous to the theoretical proton decay, the KKST process, named after the authors of (91), as follows:

$$Q + p \rightarrow Q + e^+ + \pi^0 \,. \tag{5.1}$$

The cross-section for this process, with a proton of an atom in the atmosphere molecules, increases with the Q-ball mass M_Q, and decreases with the SUSY breaking scale M_s (96)

$$\sigma_Q = 1.9 \times 10^{-36} \left(\frac{TeV}{M_s}\right)^{8/3} \left(\frac{M_Q}{GeV}\right)^{2/3} \mathrm{cm}^2 \,. \tag{5.2}$$

The neutral Q-ball breaks the proton, resulting in the emission of the energy ~ 1 GeV carried by a neutral pion and a positron, in addition to a small fraction of the Q-ball's kinect energy. (91, 100) These two particles (e^+ and π^0) will initiate typical electromagnetic air showers. The Q-ball, however, continues its trajectory, unaffected, re-interacting with protons in the atmosphere, until it touches the ground. As it propagates, more and more air showers are initiated by the KKST process, resulting in an Extensive Air Shower potentially detectable by the Pierre Auger Observatory.

5.3 Previous Works in Q-balls and Air Showers

Two main studies were already done involving Q-balls simulations applied to the Pierre Auger Observatory dataset; Dr. Mayotte's (73) and Dr. Schuster's (101) theses. The former studies slow moving and heavier Q-balls, that consequentially have bigger σ_Q, causing a larger number of proton decays, passing the Pierre Auger Observatory's FD threshold at any initial velocity. The latter studies lighter Q-balls with extremely high velocities, capable of generating detectable EAS by the Pierre Auger Observatory as initiates protons decays throughout the atmosphere. None of them were able to identify exotic air showers in the Pierre Auger Observatory dataset.

Schuster implemented the code for Q-balls interaction in CONEX, based on the lower bound limit for Q-balls given by (96)

$$M_Q > 1.0 \times 10^{21} \left(\frac{M_s}{TeV}\right)^4 \mathrm{GeV} \,. \tag{5.3}$$

Setting $M_s = 1$ GeV, Schuster obtains the lower limit of $M_Q \geq 9 \times 10^{25}$ GeV/c^2, which implies a cross-section of $\sigma_Q = 1.9 \times 10^{-22}\,\mathrm{cm}^2 = 1.9 \times 10^5$ mb. The value that was originally implemented in CONEX, however, was of $\sigma_Q = 5.0 \times 10^5$ mb, as Schuster pointed

out that it is an order-of-magnitude of the value. Differently from others studies about Q-ball, his work is interested in fast moving candidates, considering a different approach (101)

> *in which an electrically charged Q-Ball of minimum mass is accelerated to high energy by the same astrophysical processes that accelerate normal matter. The Q-Ball then loses charge as it propagates by absorbing electrons until it becomes neutral. The neutral Q-Ball then travels in a straight line to Earth where it enters the atmosphere and begins initiating protons decays.*

In his work, the energy lost by the Q-ball during a collision with a proton is $\sim 10\%$ of its kinect energy and the air showers simulations is done by using CONEX. The energy range for the primary utilized in the simulations was from 10^{21} to $10^{23}\,$eV, maintaining σ_Q and M_Q fixed in the values shown above. (101) He proposes a Bayesian analysis for identifying possible exotic candidates at Pierre Auger Observatory database.

Mayotte, differently, is interested in slow moving Q-balls. He implemented the code for Q-ball air showers to CORSIKA based on Schuster code, but removed the momentum transfer in Q-ball/proton interaction (what gave the $\sim 10\%$ energy to the pion/positron air shower), since his interest is in heavier and slow-moving Q-balls. Mayotte also varies the Q-ball's cross section and, consequently, its mass, and sets the SUSY breaking parameter to 1 TeV, to match the latest bound fluxes by (96) to Q-balls. Table 1 presents these values.

He also calculates the theoretical energy deposit for the values on the table, and the ability of the FD and SD detectors to be triggered by it. Only the four last values from Table 1 are able to trigger the detectors, giving the FD a minimum mass sensitivity of $M_Q > 9.19 \times 10^{27}$ GeV c^{-2}, if one allows the catalyse to decay of protons only. (73)

The two works presented above focused on developing methods to detect exotic air showers. Dr. Schuster, with his Bayesian method, found a composition fraction for

Table 1 – Q-ball simulation parameters utilized by Mayotte

σ_Q(barn)	M_Q(GeV c^{-2})
100×10^3	1.21×10^{24}
500×10^3	1.35×10^{25}
1×10^6	3.82×10^{26}
5×10^6	4.27×10^{27}
10×10^6	1.21×10^{28}
20×10^6	3.42×10^{28}
41.7×10^6	1.027×10^{29}

Source: Adapted from MAYOTTE. (73)

Q-balls in the Pierre Auger Observatory dataset of about 0.7% with 99% confidence for energies above 10^{19} eV. Dr. Mayotte was not able to find exotic candidates in the Pierre Auger Observatory Fluorescence Detector database. The present work will present another method to search for exotic air showers by Q-balls air showers and propose a parametrization for σ_Q based on it. With σ_Q, one can calculate M_Q simply by working with equation 5.2, after setting M_s, by

$$M_Q = (1.9 \times 10^{36} \sigma_Q / \text{cm}^2)^{3/2} \left(\frac{M_s}{\text{TeV}} \right)^4 \text{ GeV} \tag{5.4}$$

With these three values, it is possible to calculate the Q-ball radius and charge [96], giving one a glimpse of the exotic nature of the universe.

5.4 Conex Simulation of Q-ball Showers

Regarding Q-ball simulation, the software CONEX was chosen (see Chapter 3, Section 3.5) with the hadronic model of EPOS-LHC (102) for Q-ball, implemented by Dr. Schuster and SIBYLL2.3c (103, 104) for protons, given the faster simulation time (about half of time when compared with EPOS-LHC for protons). There was no difference noted between hadronic air showers simulated by EPOS-LHC and SIBYLL2.3c. In the way the interactions are implemented, the Q-ball does not loses energy via interaction with an atmospheric proton. This can be assumed, as the references of Q-ball interaction say that the energy lost by the Q-ball is negligible, as it crosses Earth's atmosphere like a bowling ball for the other particles, continuously producing neutral pions and positrons via proton decay. (91, 95, 96, 100). So, for this work, there was no energy lost by the Q-ball between each interaction.

About CONEX simulation parameters, the azimuth and zenith angles were set to 0° and 60° respectively. The parameters of minimum and maximum primary energy were set accordingly to the groups presented below.

The simulations were distributed in three groups. The first group (group I) was merely for initial comparisons between longitudinal profiles for Q-ball-induced and proton-induced EAS. 1440 events were made for each particle type, with fixed cross section for Q-ball ($\sigma_Q = 5.0 \times 10^{5.0}$ mb), and fixed energy for both primaries of $E_0 = 10^{19.0}$ eV. This energy was chosen as the lowest energy for Q-ball to generate EAS, and the cross section was chosen based on the previous works already discussed in this chapter as being the lower bound for Q-balls cross-section. (96, 101) Tables 2 to 4 summarize each simulation group parameters.

Group II consists of simulations done again for Q-balls and protons after the previous analysis on group I (see Chapter 6). The primary Q-ball was set to a primary energy fixed at $E_0 = 10^{19.0}$ eV with a variable cross section: from $5.0 \times 10^{5.0}$ to $5.0 \times 10^{8.0}$ mb, in decade steps, since there is no upper bound value for Q-ball's cross section, as

stated by (73, 96). The primary proton, on the other hand, had its primary energy varying from $10^{17.0}$ to $10^{20.0}$ eV (see Chapter 2, Section 2.2), also in decade steps. These values were chosen to search similar observables for both primaries, by comparing results from one cross-section value for Q-ball to the primary energy values for proton. Also, this variable cross section allowed to search for changes and dependencies on the observables with it. As group I, over 1400 events were made for each primary energy for proton and each cross-section for Q-ball (resulting in more than 11500 EAS events!).

Finally, the final group III was done after group II analysis, and for this group, only on Q-balls. This was done to search for changes in exotic air showers with variable primary energy. The range chosen was from $10^{19.0}$ to $10^{21.0}$ eV (following the extreme range for UHECR), with steps of half a decade, with again over 1400 simulations for each step. With all the groups combined, over 17000 EAS were simulated in about one month total — events with the highest cross-section of $5.0 \times 10^{8.0}$ mb would need more than one day each to be simulated (in order to achieve more than 1400 events, multiple CPU clusters were used).

Table 2 – Group I simulation parameters

Q-ball		Proton
$\sigma_Q(mb)$	$E_0(\text{eV})$	$E_0(\text{eV})$
$5 \times 10^{5.0}$	$10^{19.0}$	$10^{19.0}$

Source: By the author.

Table 3 – Group II simulation parameters

Q-ball		Proton
$\sigma_Q(\text{mb})$	$E_0(\text{eV})$	$E_0(\text{eV})$
$5 \times 10^{5.0}$		$10^{17.0}$
$5 \times 10^{6.0}$	$10^{19.0}$	$10^{18.0}$
$5 \times 10^{7.0}$		$10^{19.0}$
$5 \times 10^{8.0}$		$10^{20.0}$

Source: By the author.
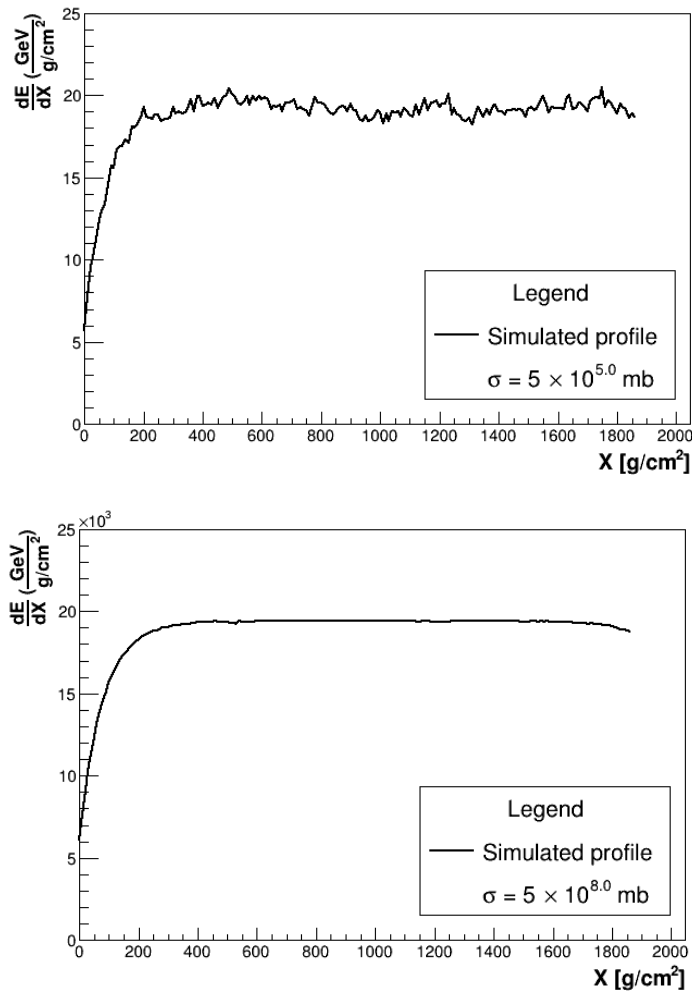
Figure 19 – Q-ball CONEX simulation for two different cross-section values.
        Source: By the author.

Table 4 – Group III simulation parameters

Q-ball	
$\sigma_Q(\text{mb})$	$E_0(\text{eV})$
	$10^{19.0}$
	$10^{19.5}$
$5 \times 10^{5.0}$	$10^{20.0}$
	$10^{20.5}$
	$10^{21.0}$

Source: By the author.

In Figure 19 we have CONEX simulation for Q-ball for two different cross-sections. It is evident a nearly constant behavior of the longitudinal profile, after a initial ascent, and that the fluctuations fall as the cross-section is increased. This decrease in the fluctuations is caused by the increase of number of interactions with a greater cross section. The
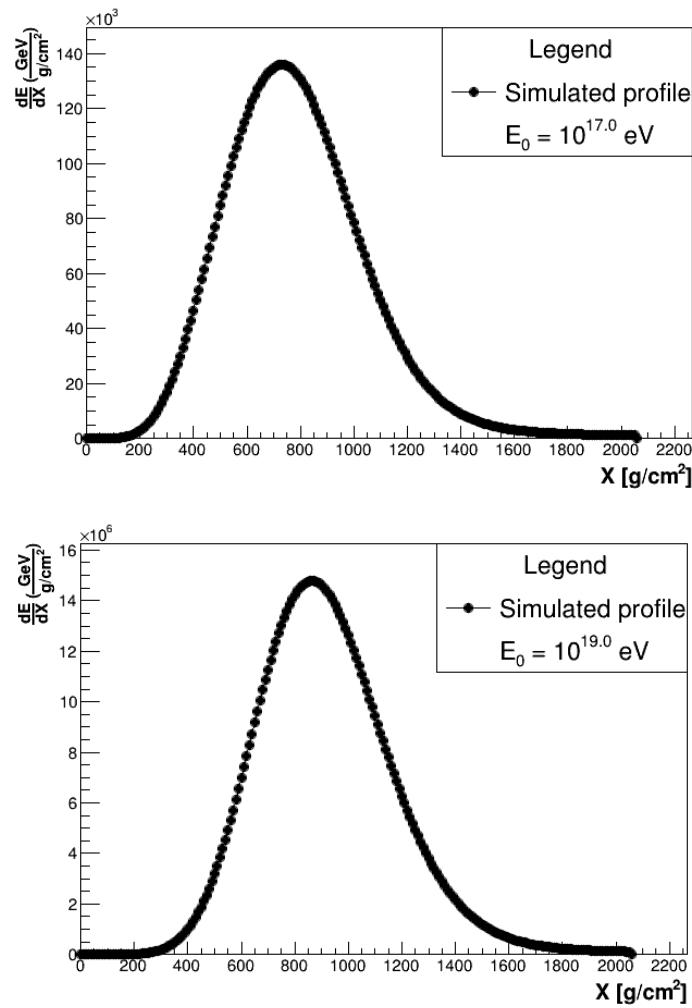
Figure 20 – Proton CONEX simulation for two different primary energy values.
Source: By the author.

constant behavior of the profile, after around 200g/cm^2, will be discussed in the next chapter.

Figure 20 presents proton simulation by CONEX for two different values of primary energy. The longitudinal profile behaves similarly for both energies, with only a small offset in X, giving a different X_{max} value. This is caused by the stochastic nature of the air shower development already addressed in this work (see Chapter 3).

One of the main questions to which this work should propose an answer is: how does one search for something that was not detected yet, relying mainly on theoretical aspects of such a thing? We already have two proposed answers for it, thanks to Drs. Schuster and Mayotte. The former, by looking for fast and light Q-balls with a Bayesian analysis, and the latter, by establishing modules and techniques at $\overline{Off}\underline{line}$ to search for slow exotic events in Pierre Auger Observatory Fluorescence Detector dataset. But in the next chapter, this work will propose an alternative answer: by looking to the shape of the

longitudinal profiles of extensive air showers.

6 EXPLORING LONGITUDINAL PROFILE SHAPE INFORMATION

When comparing Q-ball- and proton-induced air showers by their simulated longitudinal profiles, it is clear the difference between each primary (see Figures 19 and 20). But simulations provide ideal data, without any difficulties that arrive from real data measurement. In order to provide a significant classification, that can serve as a reference when working with real data, a statistical analysis should be made in order to provide a reliable method.

6.1 The χ^2 Goodness-of-Fit Method

As pointed out in the previous chapter, the statistical analysis method chosen to differentiate and classify exotic air showers from proton-induced air showers was the χ^2 value, given by goodness-of-fit test. The method consists of testing a hypothesis that proposes a fit function for a data set.

A fitted function is a function proposed to describe raw data. Its capacity of fully describing or not the data (its goodness-of-fit) is measured by the χ^2 value, (105) given by

$$\chi^2 = \sum_{i=1}^{n} \frac{(y_i - f(x_i))^2}{\sigma_i^2} \,, \tag{6.1}$$

where y_i is the raw data, in our case the simulation data, $f(x_i)$ is the proposed fit function, *e. g.* the Gaisser-Hillas function for EAS (see Figure 5) and σ_i^2 is the variance for each value. The goal of the goodness-of-fit method is to minimize the quantity $(y_i - f(x_i)/\sigma_i$ — the deviation between the ith measurement y_i and the fit function $f(x_i)$ —, meaning a good agreement between data and fit function hypothesis.

If the measured values y_i are large enough ($y_i > 5$), and if the $f(x_i)$ hypothesis is valid, then the χ^2 value will follow the χ^2 probability distribution function, with the number of degrees of freedom ndf, that is the number of measurements n minus the number of fitted parameters and variance equal to $f(x_i)$. The χ^2 becomes then *Pearson's χ^2 statistic*. This value is often divided by its number of degrees of freedom, χ^2/ndf, to normalize the value around 1. Typically, $\chi^2/ndf \approx 1$ means good agreement between data and fit function. $\chi^2/ndf << 1$ means that the fit is better than expected when comparing with the size of data errors — meaning that it does not rejects the hypothesis, but it is an indicative to check for overestimated or non-correlated errors. And finally, if $\chi^2/ndf >> 1$, then the hypothesis should be questioned. (105)

These conclusions come from the *P*-value for a given χ^2/ndf, that gives the probability that another hypothesis, fit function, would result in a χ^2 higher (*i. e.* worse) than the one obtained. To compute the *P*-value, one can use numerical solution or use
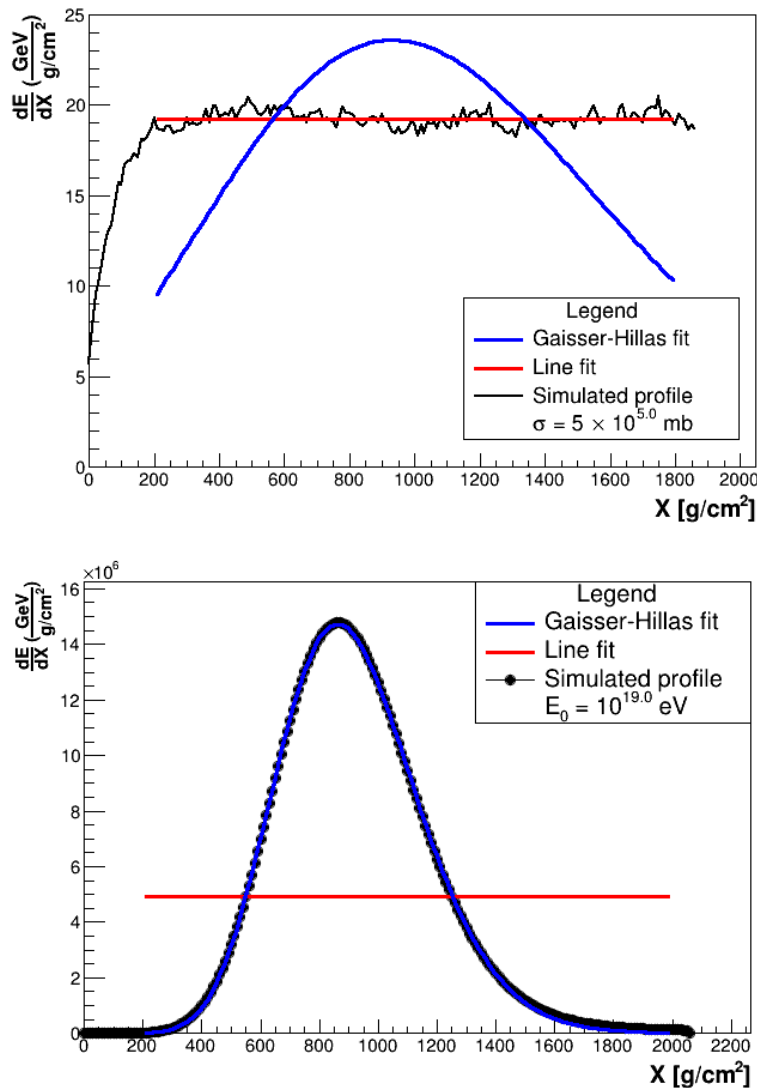
Figure 21 – Group I simulation and double fit function results. *Top*: Single Q-ball-induced Extensive Air Shower longitudinal profile with primary energy of 10^{19} eV. *Bottom*: Single proton-induced Extensive Air Shower longitudinal profile. Source: By the author.

tables and graphs found in textbooks or online. (105) Regarding these values, it should be pointed out that, even when dividing the χ^2 value by its number of degrees of freedom, the value can be greater than 1 and still be a good fit, depending on the data — the threshold for rejecting or not the hypothesis is always subjective. If the data has a large scale, even a small difference between itself and the fit function can result in a large χ^2/ndf, mainly caused by the large scale of the data — this highlights the probabilistic nature of the χ^2 value. Then, one could always apply more normalization factors to reduce data size.
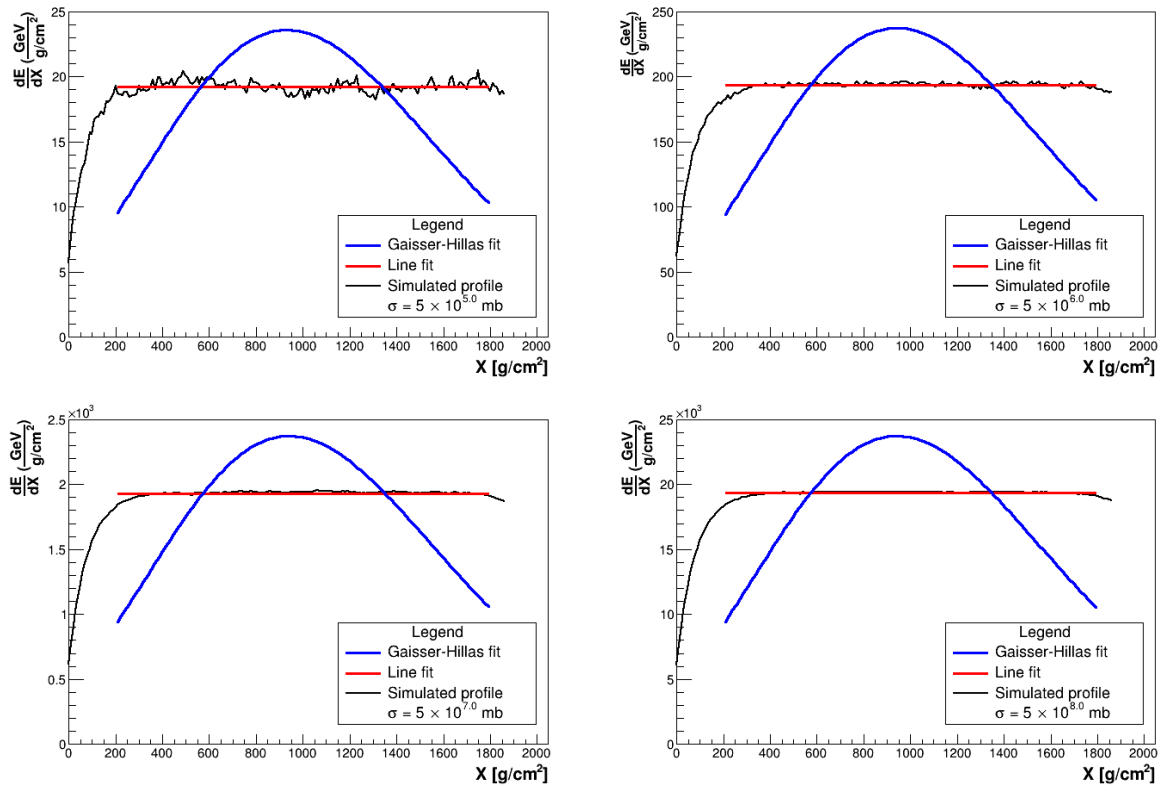
Figure 22 – Simulation group II double function fit for Q-ball simulation with variable
cross-section and fixed primary energy $E_0 = 10^{19}$ eV.
Source: By the author.

6.2 Q-ball and Proton Longitudinal Profiles Statistical Analysis

To apply the χ^2/ndf method, first is necessary to propose a hypothesis for the
data. This was done with the open-source ROOT data-analysis framework. (88) For further
details in ROOT), see (88, 106). The hypothesis initially proposed was the Gaisser-Hillas,
both for protons and for Q-balls, as is well-know for describing air shower phenomenology.
(34, 40, 56, 63)

However, after a few tests, it was clear that the Gaisser-Hillas was not appropriate
for describing an exotic air shower (see Figures 19 and 21), and based on the Q-ball air
shower longitudinal profile shape, a polynomial of degree 0 (*i.e.* a horizontal line) was
proposed.

When fitting the functions to the simulated profiles, both were fitted for both
primaries for all simulation groups and the resulting χ^2/ndf values were normalized
according for analysis. Both primaries were fitted with both functions to search for a
meaningful threshold value for classifying a longitudinal profile being exotic- or proton-
induced once double fitted by the Gaisser-Hillas and line function. This would validate
the method to be taken to the next step, that is to reconstruct all the simulation shower
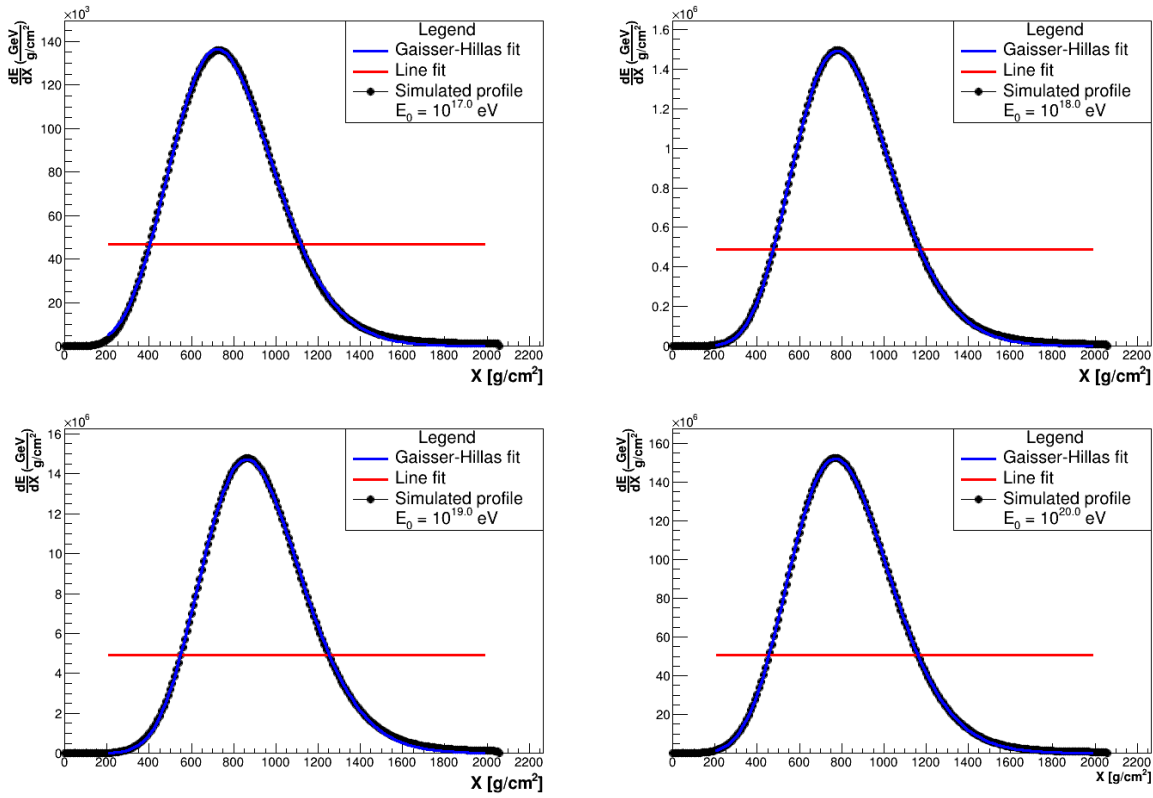
Figure 23 – Simulation group II double function fit for proton simulation with variable
primary energy.
Source: By the author.

with Pierre Auger Observatory's $\overline{\text{Off}}\underline{\text{line}}$.

For group I line function fit, the constant value was set to the mean value of the
energy deposit rate dE/dX (GeV/gcm^{-2}), and for the Gaisser-Hillas (see Equation 4.5),
both shape parameters were set according to the $\overline{\text{Off}}\underline{\text{line}}$ values for the FD reconstruction,
that is $\lambda = 61 \pm 13 \, \text{g/cm}^2$ and $X_0 = -121 \pm 172 \, \text{g/cm}^2$, being able to vary accordingly to
its respective ranges. The other two parameters of the Gaisser-Hillas, dE/dX_{max} and X_{max},
were set as the mean respectively values from the simulation events. This parameters
configuration was set for both primaries. The main goal of this first group is to check the
fit-functions behavior on both primaries, by comparing χ^2 values. After group I simulation

Table 5 – Group I χ^2/ndf results (in log(EeV/E) scale) for fitted functions, and simulation
parameters.

Q-ball			Proton		
Gaisser-Hillas fit	Line fit	σ_Q (mb)	Gaisser-Hillas fit	Line fit	E_0 (eV)
13.164 ± 0.041	8.525 ± 0.206	$5 \times 10^{5.0}$	19.574 ± 0.679	28.812 ± 0.075	$10^{19.0}$

Source: By the author.
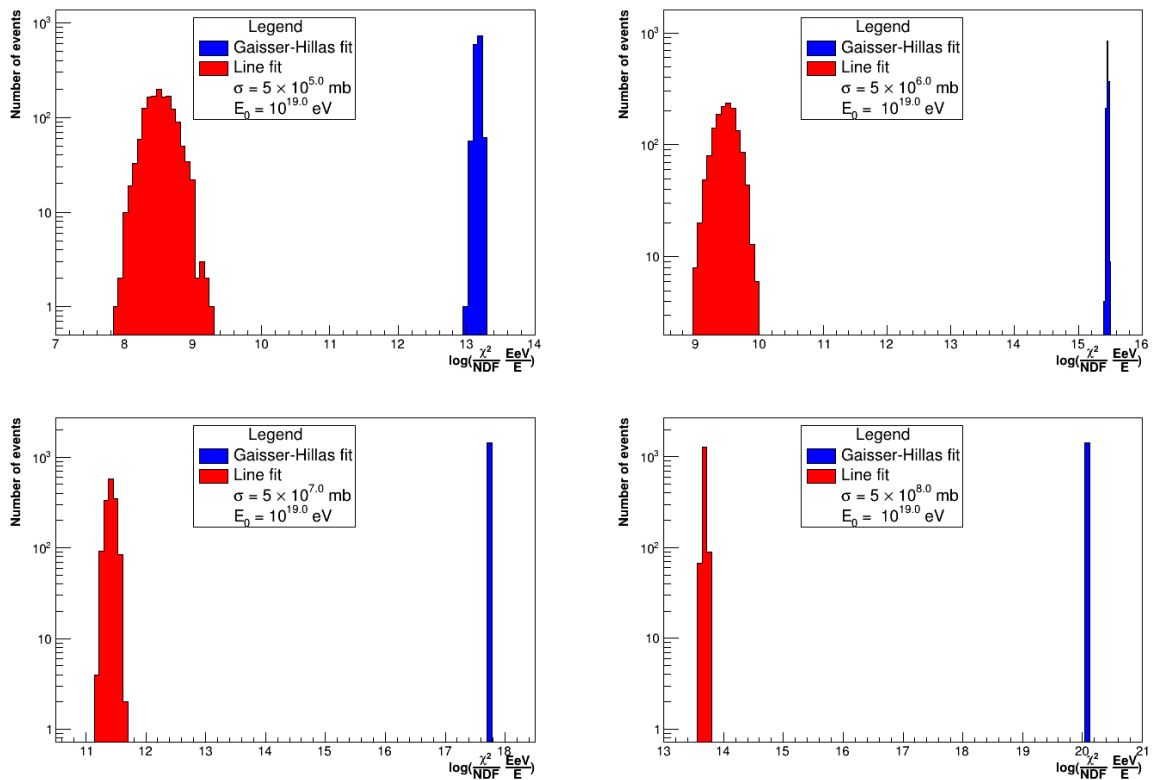
Figure 24 – Group II χ^2/ndf distribution for Q-ball-induced air showers.
Source: By the author.

analysis, it was clear that a line (with constant value in the y-axis) describes much better the exotic air shower than the Gaisser-Hillas function — and the opposite is true for the proton-induced air shower. The results for the double fitted functions can be seen in Figures 21 and for the χ^2/ndf can be seen at Table 5. The mean value of the χ^2/ndf was computed from more than 1400 EAS simulation for each primary. The scaling of the values by natural logarithm and energy (EeV/E, with E being the total deposited energy) was chosen to provide better visualization of the data — the gap between values, in reality, is much larger.

The constant value of the Q-ball air shower longitudinal profile can be intriguing at first glance, but after revisiting its interaction model with the proton, it becomes more clear: given the nature of the Q-ball interaction, and the production of the same secondaries, the longitudinal profile behaves as a constant: as it propagates, the Q-ball generates neutral pions and positrons, carrying proton's release energy of about 1 GeV. These secondaries will generate the same by-product, with the same energy, giving this constant behavior, and so on, as the Q-balls is not lost in the process. This, of course, is assumed because, in this work, the Q-ball energy lost in each interaction is disregarded (refer to Chapter 5). Also, given the field of view of a Pierre Auger telescope, the initial
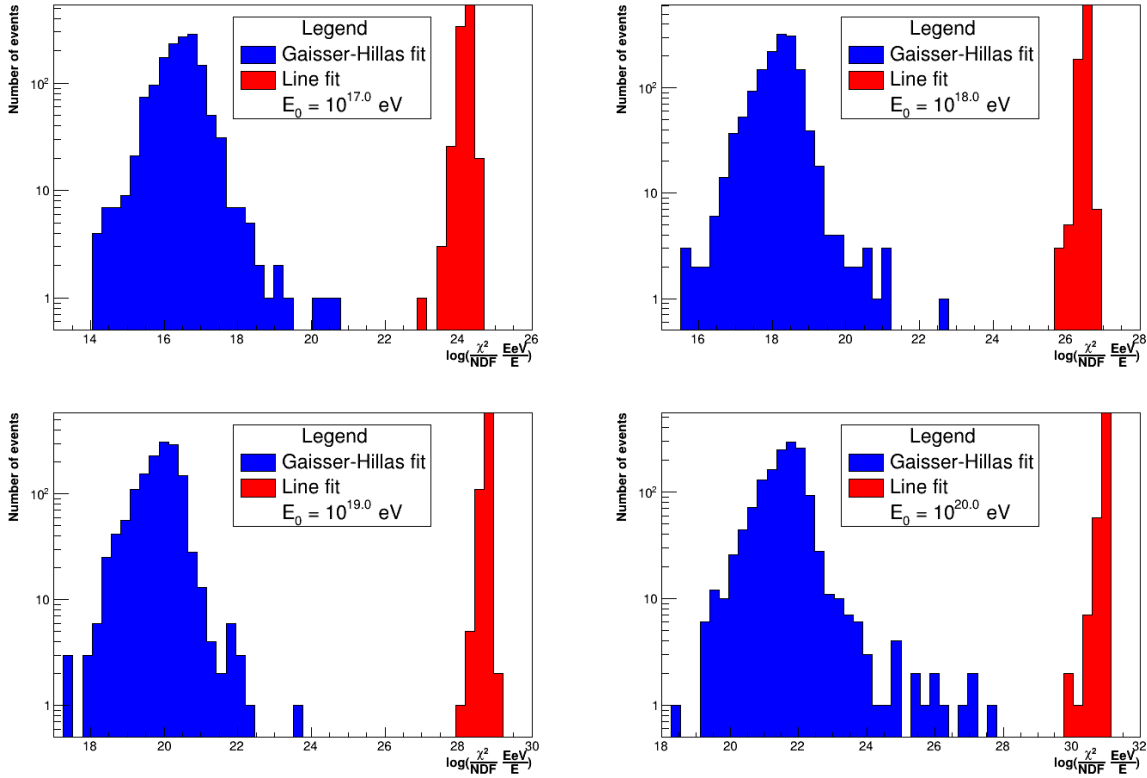
Figure 25 – Group II χ^2/ndf distribution for proton-induced air showers. Discussion about the large spread of the Gaisser-Hillas χ^2/ndf values for protons can be found on text.
Source: By the author.

ascent of the Q-ball longitudinal profile can be disregarded for the study, because it falls outside the field of view of the telescopes. This proved to be a good justification for the second hypothesis of a line being able to describe a exotic-induced air shower.

With this unambiguous classification between an exotic- and a proton-induced air shower, the group II of simulations were done. For these data, the Q-ball's cross-section σ_Q was set to four values (see Table 3) with fixed primary energy, to search for changes in the longitudinal profile with σ_Q. Also, more proton-induced air showers were simulated, this time with primary energy from $E_0 = 10^{17}$ to $E_0 = 10^{20}$ eV in decade steps, to search if both longitudinal profiles could behave similarly, leading to an erroneous classification. As can be seen in Figures 22 and 23, nothing that could resemble a similarity was found when comparing both primaries.

The χ^2/ndf values distribution can be seen in Figure 24 and 25 for both primaries. For the Q-ball distribution, there is no superposition between results — showing an unambiguously classification for an exotic air shower. For the proton distribution, the gap between distributions is not so large. The worst performance of the fitted Gaisser-Hillas
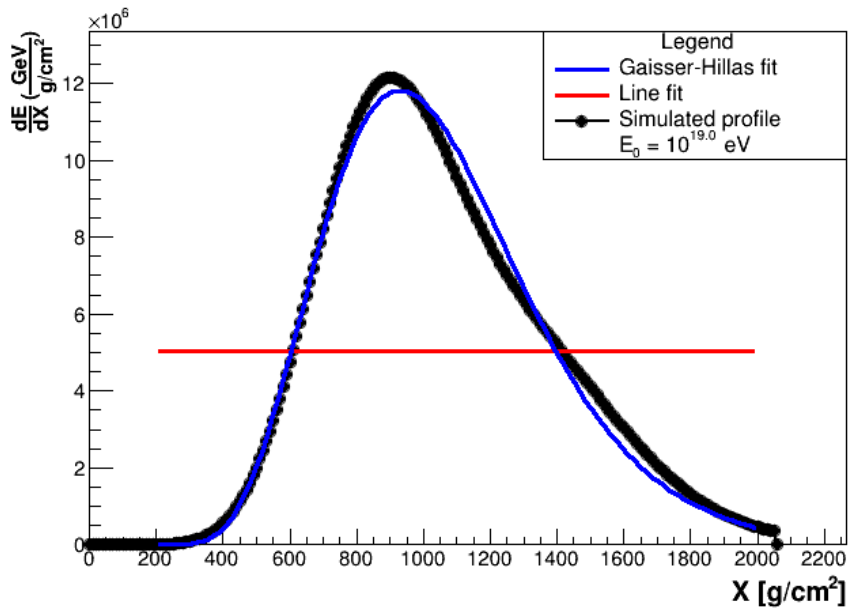
Figure 26 – Proton-induced air shower longitudinal profile with double X_{max} with Gaisser-Hillas and line fit.
Source: By the author.

function can be explained by the lower dE/dX values in both ascent and descent of the longitudinal profile for the Gaisser-Hillas function, and, in rarer cases, by uncommon EAS with double X_{max} values, as can be seen in Figure 26 — this longitudinal profile is the responsible for the highest value of χ^2/ndf for the Gaisser-Hillas fit with a primary proton of $E_0 = 10^{19}$ eV (left bottom of Figure 25). But even with this smaller gap, it is clear the classification. Table 6 summarizes the results.

With no ambiguity found between exotic- and proton-induced air showers with the classification method purely based on χ^2/ndf value given a primary energy E_0, the simulation group III was done, this time only for Q-balls, to search changes in the longitudinal profiles given different values of primary energy. As seen at Table 3, the Q-ball cross-section was fixed to $\sigma_Q = 5 \times 10^{5.0}$ mb, and its primary range was set to four values, $10^{19} \leq E_0 \leq 10^{21}$ eV in half decade steps. For each value of E_0, more than 1400 air shower

Table 6 – Group II χ^2/ndf results (in $\log{(EeV/E)}$ scale)

Q-ball			Proton		
Gaisser-Hillas fit	Line fit	σ_Q (mb)	Gaisser-Hillas fit	Line fit	E_0 (eV)
13.112 ± 0.054	8.478 ± 0.674	$5 \times 10^{5.0}$	16.436 ± 0.629	24.232 ± 0.117	$10^{17.0}$
15.456 ± 0.012	9.472 ± 0.181	$5 \times 10^{6.0}$	18.174 ± 0.596	26.517 ± 0.088	$10^{18.0}$
17.758 ± 0.004	11.420 ± 0.077	$5 \times 10^{7.0}$	19.883 ± 0.737	28.793 ± 0.071	$10^{19.0}$
20.060 ± 0.001	13.681 ± 0.025	$5 \times 10^{8.0}$	21.629 ± 0.931	31.038 ± 0.093	$10^{20.0}$

Source: By the author.
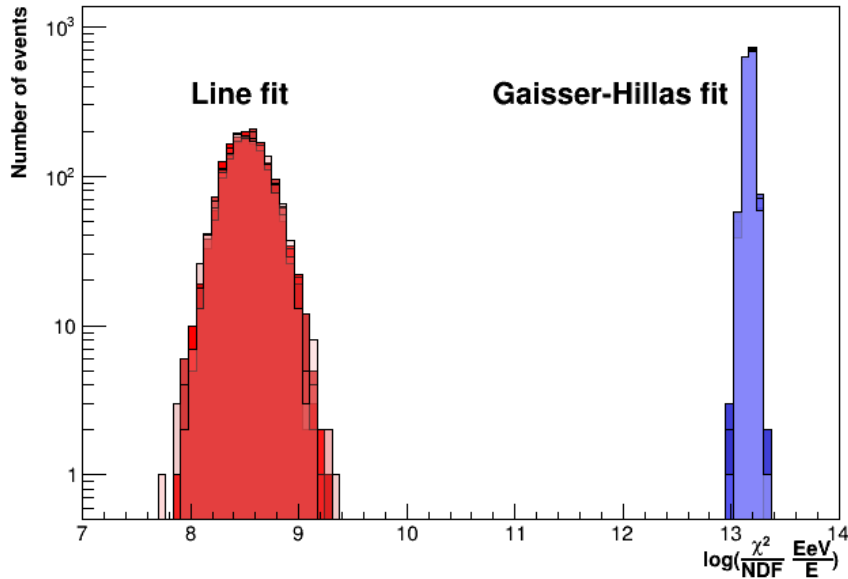
Figure 27 – Group III χ^2/ndf distribution for Q-ball air showers with different primary energy values and fixed cross-section. *Shades of red*: Five line fit χ^2/ndf values centered around 8.5. *Shades of blue*: Five Gaisser-Hillas fit χ^2/ndf values centered around 13.1
Source: By the author.

simulations were done, both of the functions were fitted and the χ^2/ndf distribution was done.

As can be seen in Figure 27, there are two overlaps of five histograms each, revealing no change in the longitudinal profile with E_0, as the χ^2/ndf values are all centered around 8.5 for the five line fit values and around 13.1 for the five Gaisser-Hillas values. Figure 28 displays the maximum energy deposit rate dE/dX_{max} distribution, with overlap of the five histograms, asserting the independence of the energy deposit rate from Q-ball air showers with different primary energies. This is expected, as there is no energy lost by the primary Q-ball in the CONEX code implementation (see Chapter 5, Section 5.4), so the only energy that is deposited arrives from the theoretical proton decay, and as it is always the same byproduct produced, depositing the same energy quantity. For these exotic-induced air showers, the energy deposit rate dE/dX has a constant behavior — minus the fluctuations that arrive from the stochastic nature of the Monte Carlo method —, so the value of dE/dX can be said to be the maximum energy deposit rate $(dE/dX)_{max}$ itself, that is, for Q-ball as primary particle:

$$\frac{dE}{dX} = \left(\frac{dE}{dX}\right)_{max}. \tag{6.2}$$

Also, given the linearity that can be observed between dE/dX and the Q-ball cross-section σ_Q values in Figure 22, a parametrization between these two quantities was proposed
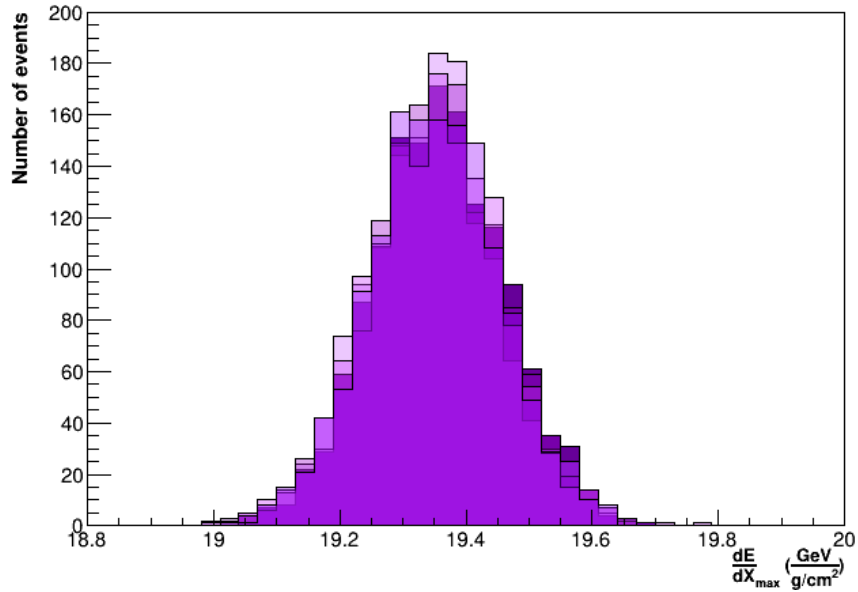
Figure 28 – Group III maximum energy deposit rate dE/dX_{max} distribution for Q-ball air showers with different primary energy values and fixed cross-section. Each one of the five violet shades histograms represents a value of Q-ball's primary energy E_0.
Source: By the author.
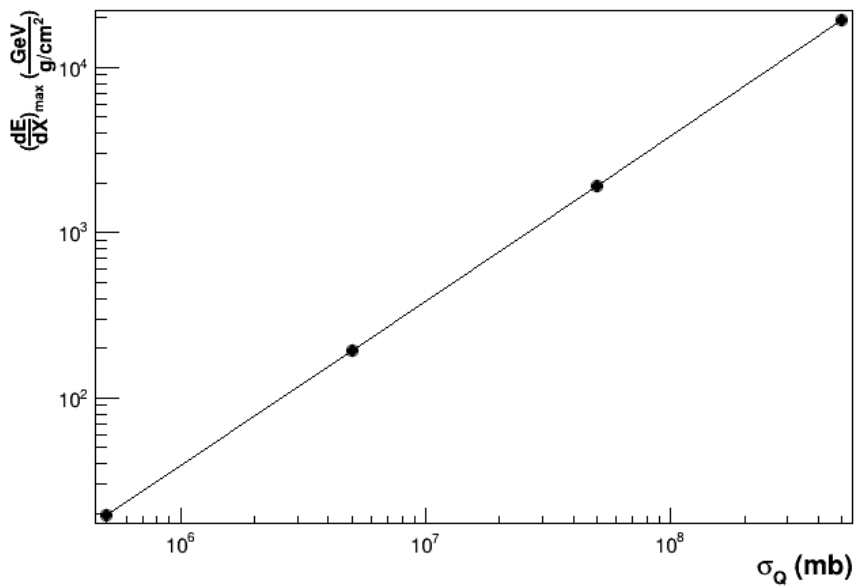
Figure 29 – Proposed parametrization based on the linearity found between maximum energy deposit rate and Q-ball cross-section. The error bars for each dot are plotted, but are too small to be noted.
Source: By the author.

(Figure 29). This allows one to write the hypothesis for Q-ball-induced showers as

$$\frac{dE}{dX} = \frac{dE}{dX}(\sigma_Q)\,, \tag{6.3}$$

and, for proton-induced air showers, we have the already confirmed Gaisser-Hillas hypothesis, that is

$$\frac{dE}{dX} = \frac{dE}{dX}\left(\left(\frac{dE}{dX}\right)_{max}, X_{max}, X_0, \lambda\right)\,. \tag{6.4}$$

From real measurements, *e.g.* Pierre Auger Observatory $\overline{\text{Off}}\underline{\text{line}}$ reconstruction data, one can obtain observables like the $(dE/dX)_{max}$. With that value, after one classifies the air shower as being an exotic air shower, one can calculate, with the proposed parametrization, the Q-ball cross-section with the air proton σ_Q, and with it, its mass M_Q (Equation 5.2) and the other parameters cited in Chapter 5, Section 5.3.

In this chapter, an unambiguous classification for exotic- and proton-induced air shower was derived along a parametrization for the former based on the energy deposit rate. Simulation group I provided the first glance at both longitudinal profiles, aligning the research: Figure 21 and Table 5 presented the results, showing the clear difference between longitudinal profiles for each primary particle. Group II established the classification method: given a longitudinal profile, when double fitting the Gaisser-Hillas and the line function, if the χ^2/ndf value is smaller for the former, it is an indicative of a proton-induced air shower, and if it is smaller for the latter, it is an indicative of a exotic-induced air shower as can be seen in Figures 22 to 25, and is summarized at Table 6. Finally, group III provided the independence of the maximum energy deposit rate $(dE/dX)_{max}$ with primary energy E_0, given the interaction process of Q-ball with an air proton (showed by Figures 27 and 28), allowing the linear parametrization of the energy deposit rate dE/dX with Q-ball cross-section σ_Q, as showed by Figure 29.

The methodology applied in this chapter will now be applied to the Pierre Auger Observatory reconstruction simulated data. This will be done in order to test the method and provide a tool to search for exotic-particle candidates in the Pierre Auger Observatory database.

7 EXPLORING LONGITUDINAL PROFILE SHAPE INFORMATION INCLUDING OBSERVATORY SIMULATION

Q-ball- and proton-induced air-shower simulations provided by algorithms such as CONEX or CORSIKA allow the exploration of the physics behind air showers with no detection effects (*i.e.* uncertainties from instrumentation). However, real air shower data, taken from observatories, comes with all of those. In this chapter, the simulated air showers are used to simulate the detector response of the telescopes of the Pierre Auger Observatory and are reconstructed using the same procedure of real data.

7.1 Simulation of the Pierre Auger Observatory

The $\overline{\text{Off}}\underline{\text{line}}$ Framework was developed by the Pierre Auger Collaboration to simulate the detector and reconstruct the primary particle properties of simulated and real data. The simulation of the detectors was implemented in details to reproduce the real operational conditions of the instruments. For this work, the limited field of view, noise and pixelization of the Fluorescence telescopes are the most important sources of uncertainties taken into account by the $\overline{\text{Off}}\underline{\text{line}}$ Framework in the simulation routines.

Figure 30 illustrates the simulation of a proton shower through the telescope — note the fluctuations and pixelization introduced by the simulation of the telescope. This figure also shows the fit of a Gaisser-Hillas profile, which is the most important reconstruction step for this work.

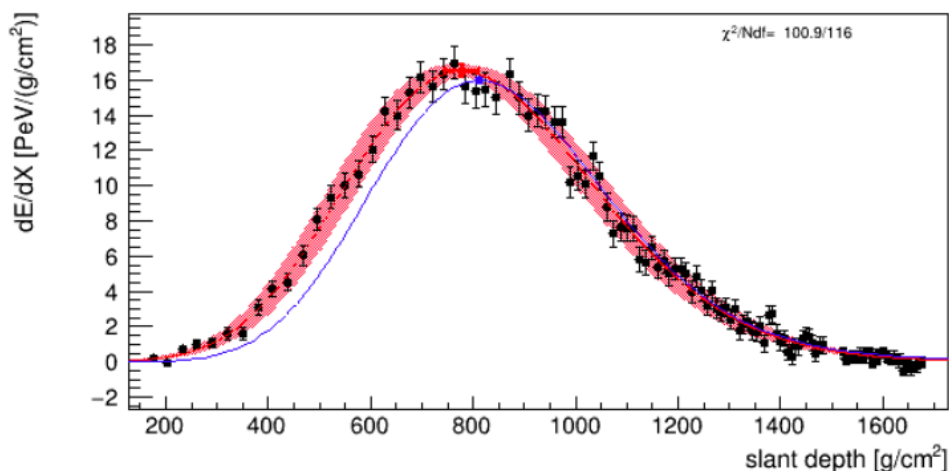Figure 30 – Proton-induced shower longitudinal profile with primary energy of $E_0 = 10^{19.0}$ eV reconstructed by Pierre Auger Observatory. Black dots corresponds to reconstructed events within the air shower. The red line corresponds to the fitted Gaisser-Hillas function, with the red hatched area being the fit error, while the blue line corresponds to the data signal.
Source: By the author.

In Figure 31 the simulation of Q-ball showers through the telescope is presented. The fit of a horizontal line is also displayed. The fit was introduced by a new module added to the $\overline{\text{Off}\underline{\text{line}}}$ Framework — more details can be found in Appendix A.

7.2 On the Identification of Q-balls

From Table 1, the lower sensibility for Q-ball events is $\sigma_Q \sim 10^9$ mb for the Observatory — Q-ball events with smaller cross sections (*e.g.* $\sigma_Q = 10^{8.0}$ mb) do not trigger the fluorescence detectors. From the previous chapter, the simulation showers would not trigger the detectors, so events with larger cross sections would be necessary. However, the simulation of events with such high value of cross section would demand an impracticable amount of simulation time — one simulated event for a higher cross-section, say $\sigma_Q = 10^{9.0}$ mb, would need a minimum of five days. To overcome this technical limitation, we resort on the linearity found between the cross section and the energy-deposit rate in the previous chapter (Figure 29) to emulate showers induced by Q-balls of larger cross sections. In practice, it is found that the energy-deposit profiles of Q-ball-induced showers are directly proportional to the Q-ball cross section, so we rescale the profiles of showers simulated with $\sigma_Q = 5 \times 10^8$ mb by a factor of 10 to obtain a sample of showers assuming a cross section also ten times larger.

This extrapolation resulted in events that triggered the Observatory in about 1/3 of the total of simulations with the Observatory (~ 450 from over 1400 events) — for simulation of events with larger cross-section, more time would be needed. And from the triggered events, only a little more than 300 were fully simulated. For protons, CONEX simulation for protons with $E_0 = 10^{19.0}$ eV were used, maintaining the same sample size as for Q-ball reconstructed events.

After performing the reconstruction of events on both primaries with the line fit, the same analysis done in Chapter 6 was performed. In Figure 32 these results can be seen and are summarized at Table 7.

As can be seen at Figure 31, the energy deposit rate dE/dX is correctly reconstructed, given the values of chapter 6 and the extrapolation by a factor of ten of the reconstructed data. The showers are only partially reconstructed, with far fewer events

Table 7 – Pierre Auger Observatory reconstruction of simulated events χ^2/ndf results (in log scale) for primary particles, and simulation parameters.

Q-ball		Proton	
Line fit	σ_Q (mb)	Line fit	E_0 (eV)
1.155 ± 0.959	$5 \times 10^{9.0}$	5.841 ± 1.088	$10^{19.0}$

Source: By the author.
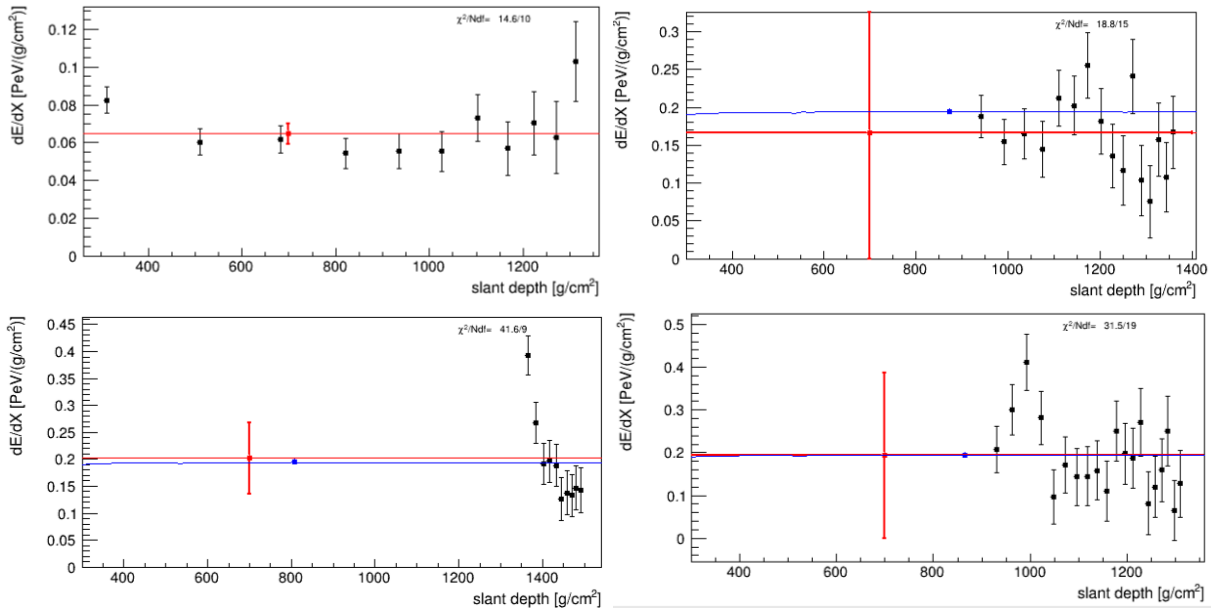
Figure 31 – Q-ball-induced showers longitudinal profiles with primary energy of $E_0 = 10^{19.0} \, eV$ and cross-section of $\sigma_Q = 5 \times 10^{9.0} \, mb$. Black dots corresponds to reconstructed events within the air shower. The red line corresponds to the fitted line function, while the blue line corresponds to the data signal.
Source: By the author.

when compared to the simulations without the telescopes (that has ~ 200 events), and those simulated with the telescopes do not follow the constant behavior observed in the previous chapter. Also, the effects of the Observatory's field of view can be seen (most events recorded only on the end of the slant depth). However, the reconstruction of the simulations by the Pierre Auger Observatory, despite the addition of all instrumental uncertainties cited before, provided successful results. Figure 32 shows the distribution of χ^2/ndf for both primaries, with an superposition of only about 5%. These results allow for the differentiation of the two primaries by the line fit function: assuming the mean value of $\log(\chi^2/ndf))$ and its standard deviation for the primary Q-ball (check Table 7), one can classify Q-ball-induced showers with 95.333% of accuracy, assuming $\log(\chi^2/ndf) = 1.155 \pm 2 \times 0.959$, with only 14 false-positives (proton-induced showers). Lowering the value to $\log(\chi^2/ndf) = 1.155 \pm 0.959$ provides no miss-classification between the two primaries, but only about 68% of Q-ball events are classified.

The values presented at Table 7 in the Line Fit columns should serve as an initial threshold value for χ^2/ndf indicative of exotic-induced air showers — in order to truly establish a threshold value, more tests should be perform.

The results presented in this chapter corroborated with the previous one, and showed a possible method to classify potential exotic-induced air showers to search for the exotic particle Q-ball at the Pierre Auger Observatory based on χ^2/ndf fit value.
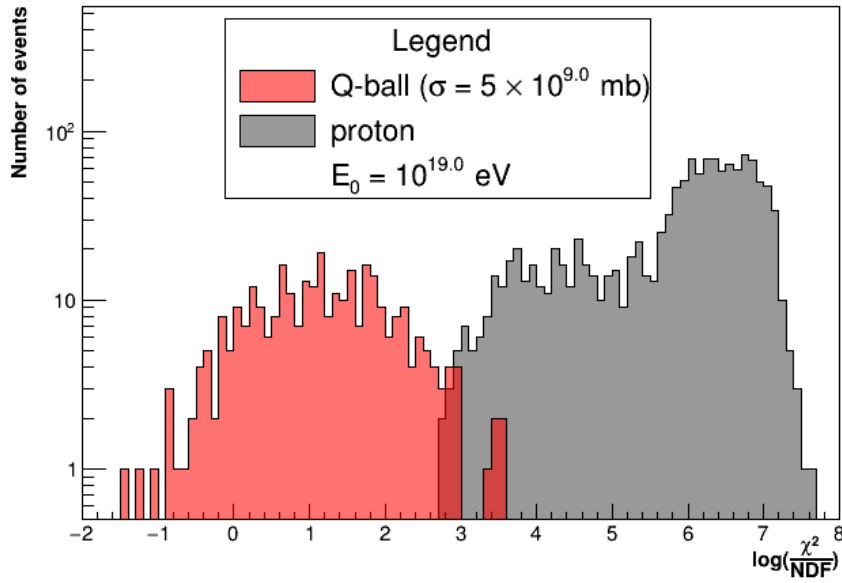
Figure 32 – χ^2/ndf distribution comparison for both primaries with the Pierre Auger Observatory reconstruction with line fit.
Source: By the author.

The proposed line fit function showed good discrimination factor for Q-ball-induced air showers with $\sigma_Q = 5 \times 10^{9.0}$ mb and $E_0 = 10^{19.0}$ eV when comparing with proton-induced air showers with the same primary energy. Next steps would include perform more tests on reconstructed events for Q-ball-induced air showers with higher cross-section, in order to establish a threshold value indicative of exotic candidates and test this value on a different dataset with mixed exotic- and proton-induced showers (a test set). Given successful metrics, one could search the Pierre Auger Observatory database for ultra-high-energy events with this proposed method and threshold value — by applying the line fit function and perform the χ^2/ndf analysis to search for values around the threshold.

8 FINAL THOUGHTS AND FUTURE PERSPECTIVES

The main purpose of this work was to study exotic-induced air showers from simulations, and develop and test a method to differentiate these events from hadronic-induced air showers by looking at the extensive air shower longitudinal profile. As a product of this research, a module was developed for the Pierre Auger Observatory $\overline{\text{Off}}\underline{\text{line}}$ capable of doing so. The module fits a line with constant y-axis value and, by comparing the fit of simulated exotic-induced air showers with proton-induced air showers, with χ^2/ndf analysis, one is able to establish a threshold value for exotic candidates — after proven efficiency. The following section outlooks and summarizes this dissertation results, followed by a final section with future perspectives to concretize the developed method.

8.1 Results Overview

First, in Chapter 5, the exotic particle Q-ball was presented as a candidate for Ultra-High-Energy Cosmic Rays, with a theoretical overview and description of its interaction model with a proton from atmospheric molecules along with previous works on Q-ball and air shower simulation. These works provided the tools for the simulation of Q-ball-induced showers and lower bounds on the Q-ball cross-section parameter for this research. With those, the Q-ball-induced air shower simulation was set for three groups, two along with proton-induced air shower simulation with the Conex algorithm. The first group, group I, was to compare the longitudinal profile from both primaries, with fixed primary energy and cross-section, and to study the proposed fit functions. Group II was to check for similarities of observables from Q-ball-induced air showers with different cross-sections and proton-induced air showers with different primary energy values. Lastly, the group III was set only for Q-ball, this time to search for changes in the longitudinal profile with variable primary energy. In total, more than 17000 air shower events were simulated.

In Chapter 6, the χ^2/ndf goodness-of-fit method was presented as the statistical method analysis for the simulations, along with the two hypothesis for it (the Gaisser-Hillas and the line fit functions) and the simulation results. These two functions were fitted first to group I longitudinal profile events, to check fit behavior and, after the results were studied, were also fitted to group II. The results, from both groups, showed an unambiguously classification for Q-ball-induced and proton-induced air showers based on the χ^2/ndf: the low values for the line fit and high values for the Gaisser-Hillas fit being an indicative of the former, and the opposite for the latter. Lastly, on group III, the longitudinal events were studied to check for changes for the energy deposit rate dE/dX with primary energy E_0 for Q-balls, with no changes found, indicating that the Q-ball-induced air shower dE/dX is function only on its cross-section σ_Q — allowing a parametrization of dE/dX_{max} with

σ_Q. This chapter consists of the first part of the results.

Finally, Chapter 7 presented the application of the proposed method for classification of Q-ball-induced air showers simulated through the Pierre Auger Observatory. For this purpose, a new $\overline{\text{Off}}\underline{\text{line}}$ module was developed capable of applying the line fit. The events simulated with this new module came from group II: Q-ball-induced air showers with highest $\sigma_Q = 10^{8.0}\,mb$ and $E_0 = 10^{19.0}\,GeV$, and proton-induced showers with the same E_0 — however, the selected cross-section was not enough to trigger the Pierre Auger Observatory, so an extrapolation was necessary, given the time-demand of higher cross-sections events. This extrapolation was derived from linearity found in the previous chapter. With the extrapolated events, the simulation was possible and provided the results showed in the chapter — corroborating with the results of the previous chapter. This allowed a initial test validation for the proposed method with successful results.

8.2 What's Next?

Regarding the next steps for this research to fully test and validate the proposed method, the first step would be to simulate more events for higher cross-sections. It is expected that the events generated by Q-balls with $\sigma_Q > 10^9\,mb$ will have a better response from the Observatory, by triggering it more. With more events reconstructed, the threshold value for classifying Q-ball-induced air showers can be tested and validated. As an example of possible test, 1000 test showers with mixed known composition (*e.g.* 50% proton-induced and 50% Q-ball-induced air showers) could be classified accordingly to the threshold value. Another way would be to establish a threshold value for a training set, and apply it on a test set and check its accuracy and efficiency — similarly to machine learning techniques.

Once validated, the proposed method would serve to search for this exotic particle at the Pierre Auger Observatory and even other observatories that operate in this high-energy end of the cosmic ray spectrum, when correctly applied.

This work provided an alternate way to search for the exotic particle Q-ball, by obtaining information from its longitudinal profile when studying air showers induced by it from simulations. The method, the analysis of χ^2/ndf values for the new proposed line fit function, although simple, showed promising results and, once validate, can serve as a tool to search for extreme and exotic events — and with those, maybe even discover new physics.

REFERENCES

1 WULF, T. On the radiation of high penetrating power that exists in the atmosphere. **Physikalische Zeitschrift**, v. 1, n. 152-157, p. 124, 1909.

2 HESS, V. F. Uber beobachtungen der durchdringenden strahlung bei sieben freiballonfahrten. **Physikalische Zeitschrift**, v. 13, p. 1084–1091, 1912.

3 MILLIKAN, R. A. Available energy. **Science**, American Association for the Advancement of Science, v. 68, n. 1761, p. 279–284, 1928.

4 CLAY, J. Results of the dutch cosmic-ray expedition 1933: briefly communicated. **Physica**, Elsevier, v. 1, n. 1-6, p. 363–382, 1934.

5 ROSSI, B. On the magnetic deflection of cosmic rays. **Physical Review**, APS, v. 36, n. 3, p. 606, 1930.

6 JOHNSON, T. H. The azimuthal asymmetry of the cosmic radiation. **Physical Review**, APS, v. 43, n. 10, p. 834, 1933.

7 ALVAREZ, L.; COMPTON, A. H. A positively charged component of cosmic rays. **Physical Review**, APS, v. 43, n. 10, p. 835, 1933.

8 ANDERSON, C. D. The positive electron. **Physical Review**, APS, v. 43, n. 6, p. 491, 1933.

9 NEDDERMEYER, S. H.; ANDERSON, C. D. Note on the nature of cosmic-ray particles. **Physical Review**, APS, v. 51, n. 10, p. 884, 1937.

10 ROSSI, B. Method of registering multiple simultaneous impulses of several geiger's counters. **Nature**, Nature Publishing Group, v. 125, n. 3156, p. 636–636, 1930.

11 MAZE, R. Étude d'un appareil à grand pouvoir de résolution pour rayons cosmiques. **Journal de Physique et le Radium**, Société Française de Physique, v. 9, n. 4, p. 162–168, 1938.

12 AUGER, P.; MAZE, R.; GRIVET-MAYER, T. Extensive cosmic showers in the atmosphere containing ultra-penetrating particles. **Comptes Rendus de l'Académie des Sciences (Série II)**, v. 206, p. 1721, 1938.

13 KAMPERT, K.-H.; WATSON, A. A. Extensive air showers and ultra high-energy cosmic rays: a historical review. **The European Physical Journal H**, Springer, v. 37, n. 3, p. 359–412, 2012.

14 LINSLEY, J.; SCARSI, L.; ROSSI, B. Extremely energetic cosmic-ray event. **Physical Review Letters**, APS, v. 6, n. 9, p. 485, 1961.

15 LINSLEY, J. Evidence for a primary cosmic-ray particle with energy 10^{20} ev. **Physical Review Letters**, APS, v. 10, n. 4, p. 146, 1963.

16 LINSLEY, J. Primary cosmic rays of energy 10^{17} to 10^{20} ev, the energy spectrum and arrival directions. *in:* international cosmic ray conference 8., 1963. **Proceedings** [...] 1963ICRC, v.4, p.77, 1963. Available from: https://articles.adsabs.harvard.edu/pdf/1963ICRC....8d..77L. Accessible at: 30 Mar. 2023.

17 BALTRUSAITIS, R. *et al.* The Utah Fly's eye detector. **Nuclear Instruments and Methods in Physics Research Section A**, Elsevier, v. 240, n. 2, p. 410–428, 1985.

18 CHIBA, N. *et al.* Akeno Giant Air Shower Array (AGASA) covering 100 km^2 area. **Nuclear Instruments and Methods in Physics Research Section A**, Elsevier, v. 311, n. 1-2, p. 338–349, 1992.

19 WINN, M. M. *et al.* The cosmic-ray energy spectrum above 10^{17}ev. **Journal of Physics G**, IOP Publishing, v. 12, n. 7, p. 653–674, July 1986. DOI: 10.1088/0305-4616/12/7/015.

20 TENNENT, R. The Haverah Park extensive air shower array. **Proceedings of the Physical Society (1958-1967)**, IOP Publishing, v. 92, n. 3, p. 622, 1967.

21 ANATOLY, I. The Yakutsk array experiment: main results and future directions. **EPJ Web of Conferences**, v. 53, p. 04003, 2013.

22 PIERRE AUGER COLLABORATION. The Pierre Auger Cosmic ray Observatory. **Nuclear Instruments and Methods in Physics Research Section A**, v. 798, p. 172–213, 2015. DOI: 10.1016/j.nima.2015.06.058.

23 KAWAI, H. *et al.* Telescope Array experiment. **Nuclear Physics B** — proceedings supplements, n. 175-176, p. 221–226, 2008. DOI: 10.1016/j.nuclphysbps.2007.11.002.

24 GREISEN, K. End to the cosmic-ray spectrum? **Physical Review Letters**, APS, v. 16, n. 17, p. 748, 1966.

25 ZATSEPIN, G. T.; KUZ'MIN, V. A. Upper limit of the spectrum of cosmic rays. **Soviet Journal of Experimental and Theoretical Physics Letters**, v. 4, p. 78, 1966.

26 ABBASI, R. *et al.* First observation of the Greisen-Zatsepin-Kuzmin suppression. **Physical Review Letters**, APS, v. 100, n. 10, p. 101101, 2008. DOI: 10.1103/PhysRevLett.100.101101.

27 ABRAHAM, J. *et al.* Observation of the suppression of the flux of cosmic rays above 4×10^{19} ev. **Physical Review Letters**, APS, v. 101, n. 6, p. 061101, 2008.

28 AAB, A. *et al.* Measurement of the cosmic-ray energy spectrum above 2.5×10^{18} ev using the Pierre Auger Observatory. **Physical Review D**, APS, v. 102, n. 6, p. 062005, 2020.

29 ABREU, P. *et al.* Interpretation of the depths of maximum of extensive air showers measured by the Pierre Auger Observatory. **Journal of Cosmology and Astroparticle Physics**, v. 2013, n. 2, p. 026, 2013. DOI: 10.1088/1475-7516/2013/02/026.

30 AAB, A. *et al.* Depth of maximum of air-shower profiles at the Pierre Auger Observatory. ii. Composition implications. **Physical Review D**, APS, v. 90, n. 12, p. 122006, 2014.

31 AAB, A. *et al.* Evidence for a mixed mass composition at the 'ankle'in the cosmic-ray spectrum. **Physics Letters B**, Elsevier, v. 762, p. 288–295, 2016. DOI: 10.1016/j.physletb.2016.09.039.

32 YUSHKOV, A. Mass composition of cosmic rays with energies above $10^{17.2}$ ev from the hybrid data of the Pierre Auger Observatory. **Proceedings of Science**, 2019. DOI: 10.22323/1.358.0482.

33 ARBELETCHE, L. B. **Simulation of extensive air showers and its detection**. 2021. Ph. D. Thesis (Science) — Instituto de Física de São Carlos, Universidade de São Paulo, São Carlos, 2021.

34 PARTICLE DATA GROUP *et al.* Review of particle physics. **Progress of Theoretical and Experimental Physics**, Oxford University Press, v. 2020, n. 8, p. 083C01, 2020.

35 ALFARO, R. *et al.* All-particle cosmic ray energy spectrum measured by the hawc experiment from 10 to 500 tev. **Physical Review D**, APS, v. 96, n. 12, p. 122001, 2017.

36 ABREU, P. *et al.* The Pierre Auger Observatory II: studies of cosmic ray composition and hadronic interaction models. *In*: INTERNATIONAL COSMIC RAY CONFERENCE, 32., 2011, Beijing. **Proceedings** [...], Beijing: ICRC, 2011. DOI: 10.7529/ICRC2011/V03/0956.

37 PERKINS, D. H. **Particle astrophysics**. 2nd ed. Oxford: Oxford University Press, 2009.

38 AAB, A. *et al.* Features of the energy spectrum of cosmic rays above 2.5× 10 18 ev using the Pierre Auger Observatory. **Physical Review Letters**, APS, v. 125, n. 12, p. 121106, 2020.

39 WORKMAN, R. L. *et al.* Review of Particle Physics. **Progress of Theoretical and Experimental Physics**, v. 2022, n. 8, Aug. 2022. DOI: 10.1093/ptep/ptac097.

40 LONGAIR, M. S. **High energy astrophysics**. 3rd ed. Cambridge: Cambridge University Press, 2010.

41 GRUPEN, C. *et al.* **Astroparticle physics**. Berlin: Springer, 2005.

42 STRONG, A. W.; MOSKALENKO, I. V.; PTUSKIN, V. S. Cosmic-ray propagation and interactions in the galaxy. **Annual Review of Nuclear and Particle Science**, v. 57, n. 1, p. 285–327, 2007. DOI: 10.1146/annurev.nucl.57.090506.123011.

43 PTUSKIN, V. Propagation of galactic cosmic rays. **Astroparticle Physics**, Elsevier, v. 39, p. 44–51, 2012.

44 BIERMANN, P. L. The origin of the highest energy cosmic rays. **Journal of Physics G**, IOP Publishing, v. 23, n. 1, p. 1, 1997.

45 SARAZIN, F. *et al.* **What is the nature and origin of the highest-energy particles in the universe?** 2019. DOI: 10.48550/arXiv.1903.04063.

46 DELIGNY, O. Cosmic rays around 10^{18} eV: implications of contemporary measurements on the origin of the ankle feature. **Comptes Rendus Physique**, Elsevier, v. 15, n. 4, p. 367–375, 2014.

47 CAZON, L.; THE PIERRE AUGER COLLABORATION. Studying the nuclear mass composition of ultra-high energy cosmic rays with the Pierre Auger Observatory. **Journal of Physics (Conference Series)**, v. 375, n. 5, p. 052003, 2012.

48 IVANOV, D. Energy spectrum measured by the telescope array. *In:* INTERNATIONAL COSMIC RAY CONFERENCE, 36., 2019, Madison. **Proceedings** [...], Madison: ICRC, 2019.

49 AAB, A. *et al.* Combined fit of spectrum and composition data as measured by the Pierre Auger Observatory. **Journal of Cosmology and Astroparticle Physics**, IOP Publishing, v. 2017, n. 04, p. 038–038, April 2017. DOI: 10.1088/1475-7516/2017/04/038.

50 HAUNGS, A. *et al.* The kascade cosmic-ray data centre kcdc: granting open access to astroparticle physics research data. **The European Physical Journal C**, Springer, v. 78, n. 9, p. 1–16, 2018.

51 ENGEL, R.; HECK, D.; PIEROG, T. Extensive air showers and hadronic interactions at high energy. **Annual Review of Nuclear and Particle Science**, Annual Reviews, v. 61, p. 467–489, 2011.

52 KAMPERT, K.; UNGER, M. Measurements of the cosmic ray composition with air shower experiments. **Astroparticle Physics**, Elsevier, v. 35, n. 10, p. 660–678, 2012.

53 KNAPP, J.; HECK, D.; SCHATZ, G. Comparison of hadronic interaction models used in air shower simulations and of their influence on shower development and observables. **Forschungszentrum Karlsruhe Report**, v. 5828, 1996.

54 HECK, D. The CURVED version of the air shower simulation program CORSIKA. **Wissenschaaftliche Berichte Helmholtz-Gemeinschaft**, v. 6954, 2004.

55 STANEV, T. Cosmic rays and extensive air showers. *In:* INTERNATIONAL CONFERENCE ON ELASTIC AND DIFFRACTIVE SCATTERING, 13., 2009, Geneva. **Proceedings** [...], Geneva: EDS, 2010.

56 GAISSER, T. K.; HILLAS, A. M. Reliability of the method of constant intensity cuts for reconstructing the average development of vertical showers. *In:* INTERNATIONAL COSMIC RAY CONFERENCE, 15., 1977, Plovdiv. **Proceedings** [...], Plovdiv: ICRC, 1977.

57 GREISEN, K. Cosmic ray showers. **Annual Review of Nuclear Science**, v. 10, n. 1, p. 63–108, 1960.

58 KAMATA, K.; NISHIMURA, J. The lateral and the angular structure functions of electron showers. **Progress of Theoretical Physics Supplement**, Oxford Academic, v. 6, p. 93–155, 1958.

59 ROSSI, B.; GREISEN, K. Cosmic-ray theory. **Reviews of Modern Physics**, APS, v. 13, n. 4, p. 240, 1941.

60 FADHEL, K. F. *et al.* Estimating the lateral distribution of high energy cosmic ray particles by depending on Nishimura-Kamata-Greisen function. **Journal of Physics**: conference series, v. 1879, n. 3, p. 032089, 2021.

61 HEITLER, W. **The Quantum theory of radiation**. 3rd ed. Clarendon: Oxford University Press, 1954.

62 CARLSON, J.; OPPENHEIMER, J. On multiplicative showers. **Physical Review**, APS, v. 51, n. 4, p. 220, 1937.

63 GAISSER, T. K.; ENGEL, R.; RESCONI, E. **Cosmic rays and particle physics**. 2nd ed. Cambridge: Cambridge University Press, 2016.

64 GREISEN, K. The extensive air showers. **Progress in Cosmic Ray Physics**, North Holland, v. 3, n. 1, 1956.

65 MATTHEWS, J. A Heitler model of extensive air showers. **Astroparticle Physics**, Elsevier, v. 22, n. 5-6, p. 387–397, 2005.

66 ARBELETCHE, L.; GONÇALVES, V.; MÜLLER, M. Investigating the influence of diffractive interactions on ultrahigh-energy extensive air showers. **International Journal of Modern Physics A**, World Scientific, v. 33, n. 26, p. 1850153, 2018.

67 MEURER, C. *et al.* Muon production in extensive air showers and its relation to hadronic interactions. **Czechoslovak Journal of Physics**, Springer, v. 56, n. 1, p. A211–A219, 2006.

68 LINSLEY, J. Structure of large air showers at depth 834 g/sq cm. III-applications. *In:* INTERNATIONAL COSMIC RAY CONFERENCE, 15., 1977, Plovdiv. **Proceedings** [...], Plovdiv: ICRC, 1977.

69 GAISSER, I.; MCCOMB, T.; TURVER, K. Elongation rate of air showers and implications for $10^{17} - 10^{18}$ eV particle interactions. *In:* INTERNATIONAL COSMIC RAY CONFERENCE, 16., 1979, Kyoto. **Proceedings** [...], Kyoto: ICRC, 1979.

70 ALVAREZ-MUNIZ, J. *et al.* Hybrid simulations of extensive air showers. **Physical Review D**, APS, v. 66, n. 3, p. 033011, 2002.

71 BERGMANN, T. *et al.* One-dimensional hybrid approach to extensive air shower simulation. **Astroparticle Physics**, Elsevier, v. 26, n. 6, p. 420–432, 2007.

72 HECK *et al.* Corsika: A Monte Carlo code to simulate extensive air showers. **Forschungszentrum Karlsruhe Report**, v. 6019, n. 11, 1998.

73 MAYOTTE, E. W. **Searching for slow-developing cosmic-ray showers:** looking for evidence of exotic primaries at the Pierre Auger Observatory. 2016. Ph. D. Thesis (Science) — Colorado School of Mines, Golden, Colorado, 2016.

74 PIEROG, T. *et al.* First results of fast one-dimensional hybrid simulation of eas using conex. **Nuclear Physics B** — proceedings supplements, 2005. DOI: 10.1016/j.nuclphysbps.2005.07.029.

75 LAKEL, G.; TALAI, M. C. Ultra high energy cosmic rays simulated with conex code. **EPJ Web of Conferences**, v. 210, p. 02014, 2019.

76 SUOMIJARVI, T. **Performance of the Pierre Auger Observatory surface detector**. 2007. Available from: https://arxiv.org/pdf/0709.1823.pdf. Accessible at: 22 Mar. 2023.

77 ARGIRO, S. *et al.* The offline software framework of the Pierre Auger Observatory. **Nuclear Instruments and Methods in Physics Research Section A**, Elsevier, v. 580, n. 3, p. 1485–1496, 2007.

78 GORA, D. The Pierre Auger Observatory: review of latest results and perspectives. **Universe**, MDPI, v. 4, n. 11, p. 128, 2018.

79 MARIS, I. C. The AMIGA infill detector of the Pierre Auger Observatory: performance and first data. *In*: INTERNATIONAL COSMIC RAY CONFERENCE, 32., 2011, Beijing. **Proceedings [...]**, Beijing: ICRC, 2011.

80 THE PIERRE AUGER COLLABORATION. The Pierre Auger cosmic ray observatory. **Nuclear Instruments and Methods in Physics Research Section A**, Elsevier, v. 798, p. 172–213, 2015.

81 ALLEKOTTE, I. *et al.* The surface detector system of the Pierre Auger Observatory. **Nuclear Instruments and Methods in Physics Research Section A**, Elsevier, v. 586, n. 3, p. 409–420, 2008.

82 SHELLARD, R. C. First results from the Pierre Auger Observatory. **Brazilian Journal of Physics**, SciELO Brasil, v. 36, p. 1184–1193, 2006.

83 ABRAHAM, J. *et al.* Trigger and aperture of the surface detector array of the Pierre Auger Observatory. **Nuclear Instruments and Methods in Physics Research Section A**, Elsevier, v. 613, n. 1, p. 29–39, 2010.

84 AAB, A. *et al.* Reconstruction of events recorded with the surface detector of the Pierre Auger Observatory. **Journal of Instrumentation**, IOP Publishing, v. 15, n. 10, p. P10021–P10021, Oct. 2020. DOI: 10.1088/1748-0221/15/10/p10021.

85 ABRAHAM, J. *et al.* The fluorescence detector of the Pierre Auger Observatory. **Nuclear Instruments and Methods in Physics Research Section A**, Elsevier, v. 620, n. 2-3, p. 227–251, 2010.

86 KUEMPEL, D.; KAMPERT, K.-H.; RISSE, M. Geometry reconstruction of fluorescence detectors revisited. **Astroparticle Physics**, Elsevier, v. 30, n. 4, p. 167–174, 2008.

87 AAB, A. *et al.* Data-driven estimation of the invisible energy of cosmic ray showers with the Pierre Auger Observatory. **Physical Review D**, APS, v. 100, n. 8, p. 082003, 2019.

88 BRUN, R.; RADEMAKERS, F. Root—an object oriented data analysis framework. **Nuclear Instruments and Methods in Physics Research Section A**, Elsevier, v. 389, n. 1-2, p. 81–86, 1997.

89 LOPES, A.; PERREY, M. L. **FAQ-LHC The guide**. 2022. Available from: https://cds.cern.ch/record/2809109. Accessible at: 27 July 2022.

90 TAYLOR, F. E. **Comparison of cosmic ray flux at $\sqrt{s} \geq 14$ TeV with LHC luminosity**. 2008. DOI: 10.48550/arXiv.0805.4528.

91 KUSENKO, A. *et al.* Experimental signatures of supersymmetric dark-matter q-balls. **Physical Review Letters**, APS, v. 80, n. 15, p. 3185, 1998.

92 MAURIN, D.; TAILLET, R. Spatial origin of galactic cosmic rays in diffusion models-ii. exotic primary cosmic rays. **Astronomy & Astrophysics**, EDP Sciences, v. 404, n. 3, p. 949–958, 2003.

93 CHEN, H. *et al.* Search for new massive particles in cosmic rays. **Physics Reports**, Elsevier, v. 282, n. 1, p. 1–34, 1997.

94 KUSENKO, A.; SHAPOSHNIKOV, M. Supersymmetric q-balls as dark matter. **Physics Letters B**, Elsevier, v. 418, n. 1-2, p. 46–54, 1998.

95 BAKARI, D. *et al.* **Magnetic monopoles, nuclearites, Q-balls**: a qualitative picture. 2000. Available from: https://arxiv.org/pdf/hep-ex/0004019.pdf. Accessible at: 22 Mar. 2023.

96 ARAFUNE, J. *et al.* Experimental bounds on masses and fluxes of nontopological solitons. **Physical Review D**, APS, v. 62, n. 10, p. 105013, 2000.

97 COLEMAN, S. Q-balls. **Nuclear Physics B**, Elsevier, v. 262, n. 2, p. 263–283, 1985.

98 FRIEDBERG, R.; LEE, T.; SIRLIN, A. Class of scalar-field soliton solutions in three space dimensions. **Physical Review D**, APS, v. 13, n. 10, p. 2739, 1976.

99 LEE, T.; PANG, Y. Nontopological solitons. **Physics Reports**, Elsevier, v. 221, n. 5-6, p. 251–350, 1992.

100 BAKARI, D. *et al.* Energy losses of q-balls. **Astroparticle Physics**, Elsevier, v. 15, n. 1, p. 137–147, 2001.

101 SCHUSTER, D. **Searching for exotic particles at the Pierre Auger Observatory using Bayesian inference**. 2011. Ph. D. Thesis (Science) — Colorado School of Mines, Golden, Colorado, 2011.

102 PIEROG, T.; WERNER, K. Muon production in extended air shower simulations. **Physical Review Letters**, APS, v. 101, n. 17, p. 171101, 2008.

103 AHN *et al.* Cosmic ray interaction event generator SIBYLL 2.1. **Physical Review D**, APS, v. 80, n. 9, p. 094003, 2009.

104 FEDYNITCH, A. *et al.* Hadronic interaction model sibyll 2.3 c and inclusive lepton fluxes. **Physical Review D**, APS, v. 100, n. 10, p. 103018, 2019.

105 COWAN, G. **Statistical data analysis**. Oxford: Oxford University Press, 1998.

106 ANTCHEVA, I. *et al.* Root—a c++ framework for petabyte data storage, statistical analysis and visualization. **Computer Physics Communications**, Elsevier, v. 182, n. 6, p. 1384–1385, 2011.

APPENDIX

APPENDIX A – THE PIERRE AUGER OBSERVATORY LINE FIT MODULE

At Pierre Auger Observatory $\overline{\text{Off}}\underline{\text{line}}$, all events are reconstructed assuming that they are described by the Gaisser-Hillas function, (77) given the good agreement between experimental hadronic air shower data. In order to search for exotic air showers, the line fit function is necessary, given the results in the Chapters 6 and 7.

Given the $\overline{\text{Off}}\underline{\text{line}}$ Framework's structure, one can easily modify modules and add new ones (see Chapter 4, Section 4.4). For the purpose of this work, a new module was added, based on the `FdEnergyDepositFinderKG`, the `QBallProfileFitterKG`. This new module is essentially a copy of the `FdEnergyDepositFinderKG`, with a modified function to fit the reconstructed data — being a line — and other adjustments (like removing the invisible energy portion since Q-ball air shower does not produce muons). In Figure 33 it is shown the module sequence for fitting the line function to the event. This module would be called after the simulation of signal by the $\overline{\text{Off}}\underline{\text{line}}$ `FDSimulation` module, would made the fit for any primary particle (despite the module name), and the χ^2/ndf value would be recorded by a separated script for later analysis.

To test the `QBallProfileFitterKG` module, multiple runs were made, with reconstructed events from the simulation for protons and Q-balls used in Chapter 6 to check if it would produce the observables and χ^2/ndf values.

```
<module> EventFileReaderOG      </module>
<module> EventCheckerOG         </module>

<module> FdCalibratorOG         </module>

<module> FdPulseFinderOG        </module>
<module> PixelSelectorOG        </module>
<module> FdSDPFinderOG          </module>
<module> FdAxisFinderOG         </module>
<module> FdApertureLightKG      </module>
<module> QBallProfileFitterKG   </module>

<module> RecDataWriterNG        </module>
```

Figure 33 – Example of modules sequence for line fit, with the `QBallProfileFitterKG` module replacing the Gaisser-Hillas fit module.
Source: By the author.